Comparison of the morphology and HDS activity of ternary Co-Mo-W catalysts supported on P-modified SBA-15 and SBA-16 substrates

R. Huirache-Acuña [a,*], B. Pawelec [b], E. Rivera-Muñoz [a], R. Nava [c], J. Espino [d], J.L.G. Fierro [b]

[a] Centro de Física Aplicada y Tecnología Avanzada, Universidad Nacional Autónoma de México, A.P. 1-1010 Querétaro, Qro. C.P. 76000, Mexico
[b] Instituto de Catálisis y Petroleoquímica, CSIC, c/Marie Curie 2, Cantoblanco, 28049 Madrid, Spain
[c] Facultad de Ingeniería, Universidad Autónoma de Querétaro, Centro Universitario, Cerro de las campanas, 76010, Querétaro, Mexico
[d] Facultad de Ingeniería Química, Universidad Michoacana de San Nicolás de Hidalgo, Ciudad Universitaria, 58060, Morelia, Michoacán, Mexico

ABSTRACT

Phosphate-loaded mesoporous SBA-15 and SBA-16 materials were used as supports of novel ternary Co-Mo-W hydrodesulfurization catalysts. The effects of support morphology (SBA-15 against SBA-16) and its modification with variable amounts of phosphorus were studied. The sulfided catalysts were tested in a reaction of hydrodesulfurization (HDS) of dibenzothiophene (DBT) at 350 °C and 3.1 MPa of total H_2 pressure. The calcined, fresh sulfided and spent catalysts were characterized by a variety of techniques (N_2 adsorption–desorption isotherms, XRD, TPR, TPD-NH_3, DRS UV–vis, micro-Raman spectroscopy, XPS, HRTEM and TPO/TGA). Regardless of the support, it was found that the presence of phosphorous inhibited the HDS activity, and the catalytic response of both SBA-15- and SBA-16-based systems did not depend on the support morphology. In terms of the reaction rate constants (k), both CoMoW/SBA-15 and CoMoW/SBA-16 catalysts were more active than a CoMo/Al_2O_3 commercial catalyst containing a small amount of phosphorous in its formulation. In general, the spent CoMoW/(x)P-SBA-16 catalysts showed a lower coke formation than their SBA-15-based counterparts because the phosphate incorporation to the SBA-16 material led to decrease in coke formation in the final catalysts, as opposite to the behavior of SBA-15-based counterparts.

1. Introduction

The hydrotreatment of middle distillates is an important process in the petrochemical industry [1]. Typically, the hydrotreatment reactions are catalyzed by Co(Ni)Mo(W) catalysts supported on alumina [2]. The origin of the almost exclusive use of alumina as support has been ascribed to its outstanding textural and mechanical properties and its relatively low cost [3]. However, the evidence of a very strong metal–support interaction has urged numerous studies devoted to new supports [3]. Thus, more recently, the research concerning the development of highly dispersed phase in zeolites and mesoporous materials has been very active due to the stringent regulations concerning the maximal amount of sulfur admitted in fuels. Some results have been presented in reviews and papers concerning the effect of support in hydrotreating catalysts for ultra clean fuels [2–5].

Since the alumina-supported catalysts possess moderate acidity, it is a common practice to enhance its acidity by the surface grafting with H_3PO_4 [6]. However, literature reports suggest that the phosphorous effect depends on its content,

nature of phosphorous precursor, method of phosphorous introduction and pH of preparative solution [6]. All those factors might affect the following aspects of the final catalyst: (i) its structural and textural properties (S_{BET}); (ii) its thermal stability; (iii) the distribution between the different Co and Mo structures in the oxide precursors; and/or (iv) the morphology of MoS_2 and "Co-Mo-S" type structures formed after precursor sulfidation [2,6]. However, it is well known that the addition of phosphorous to alumina-supported catalysts has a non-linear effect on the catalytic activity. Thus, it was found that incorporation of a large amount of phosphorous (>0.6 wt%) led to decrease in the HDS activity of hydrotreating catalysts. This is because of a weakening of the interaction of the Mo phase with the altered support resulting in lower dispersion of the Mo phase [6].

As compared with alumina [[6] and references therein], the effect of phosphate incorporation on the siliceous materials was much less studied [7–12]. Recently, the generation of acidity on mesoporous silica materials such as hexagonal mesoporous silicas (HMS) [7,8] and Ti-HMS [9–12] by modification of silica surfaces with –PO_3H_2 groups has been intensively studied. This is because their interesting textural properties such as the large specific surface areas (above 1000 $m^2 g^{-1}$), uniform-sized pores (about 4 nm), thick framework walls, small crystallite size of primary particles and complementary

* Corresponding author. Tel.: +52 442 238 11 43; fax: +52 442 238 11 65.
E-mail address: rafael_huirache@yahoo.it (R. Huirache-Acuña).

textural porosity [13,14]. Thus, their wide pore openings are expected to minimize the mass transfer problems of bulky reactants and products, which may be encountered in other materials such as zeolites [14]. It was found that the $Co_3Mo_{10}/P/HMS$ sample show a drop in HDS activity with respect to Co_3Mo_{10}/HMS sample due to the strong decrease in the specific surface area and a large surface concentration of unsulfided Co^{2+} species after phosphate incorporation [8]. The increase in total metal content from 13 to 19.5 wt% ($Co_{4.5}Mo_{15}/P/HMS$) was required as to reach a little better DBT conversion than that achieved with a commercial $CoMoP/Al_2O_3$ catalyst [8]. On the contrary, an increase in activity in HDS of DBT was observed over binary CoMo catalysts once P was added to a Ti-modified HMS substrate (HMS-Ti) [10]. In this case, all P-containing catalysts recorded greater activity than their P-free counterparts because the presence of phosphorus on the support surface forced the formation of octahedral Co^{2+} species and irregular oxide Mo^{6+} particles. From the activity–structure analysis, it was concluded that optimum P-loading in the CoMo/P-HMS-Ti systems is achieved at 0.64 wt% of P_2O_5. For the HDS of 4,6-dimethyldibenzothiophene on those catalysts [9], it was demonstrated that both activity and selectivity depend largely on the presence of Brønsted acid sites as well as on the total amount of Brønsted and Lewis acid sites. Some clues on the enhancement of activity and isomerization observed with the catalyst prepared by simultaneous impregnation and modified with P was related to the cumulative effects of the lower size of MoS_2 slabs and their higher surface density, as revealed from HR-TEM analyses [9].

As compared with the HMS, both SBA-15 and SBA-16 substrates are more stable due their thicker pore walls [8]. However, as far as we know the effect of phosphate incorporation onto these materials is not reported in literature. The morphology of the SBA-15 and SBA-16 materials is very different. On the one hand, the SBA-15 possesses hexagonal pores in a 2D array with long 1D channels (P6 mm plane group) [15]. On the other hand, the SBA-16 has a 3D cubic arrangement of mesopores corresponding to Im3m space group symmetry [16]. For this material, high-resolution electron microscopy demonstrated that each mesopore in the body-centred cubic array is connected with its eight neighbors [17]. This provides more favorable mass transfer than in the unidirectional pore system of other hexagonal mesoporous materials such as SBA-15 [18]. This prompts us to compare the effect of phosphate incorporation into both SBA-15 and SBA-16 materials.

In this work, the effect of phosphate incorporation and support morphology (SBA-15 vs. SBA-16) on HDS activity of ternary Co-Mo-W catalysts has been studied. As far as we know both effects are not yet reported in literature. The calcined, sulfided and spent catalysts have been characterized by variety of techniques (XRD, S_{BET}, TPR, TPD-NH$_3$, DRS UV–vis, micro-Raman spectroscopy, XPS, HRTEM and TPO/TGA). The sulfided catalysts were tested in the hydrodesulfurization (HDS) of dibenzothiophene (DBT) performed in a batch reactor. This reaction was selected for the catalyst screening because DBT is a typical sulfur-containing hydrocarbon present in the petroleum fraction of high-boiling oil or coal derived liquids [2] and the absence of any diffusion limitation for DBT molecule to entry into the porous structure of the SBA-15 and SBA-16-supported catalysts (DBT molecule covers surface area of 8.0×12.2 Å^2). Indeed, a laboratory-scale catalyst's activities screening in the HDS of DBT have been frequently performed in pressurized flow [19] and batch reactors [20–26].

2. Experimental

2.1. Support preparation

The siliceous SBA-15 and SBA-16 mesoporous materials were synthesized according to the procedure described by Flodström

and Alfredsson [27]. For the synthesis of SBA-15 material, Pluronic P123 (EO$_{20}$PO$_{70}$EO$_{20}$, BASF) was used as the structure directing agent. Typically, the Pluronic P123 was dissolved in a solution of water and HCl 4 M under stirring. After this, the required amount of tetraethyl orthosilicate (TEOS, 98%, Aldrich) was added to the solution, which was stirred at 35 °C for 24 h. The mixture was subsequently transferred into polypropylene bottles and heated at 80 °C for 24 h. After this, the solid obtained was filtered, washed thoroughly with deionized water, dried first in air at room temperature and then to 110 °C for 18 h and calcined at 500 °C for 6 h in order to remove the organic template.

A very similar procedure was used to synthesize the SBA-16 support where Pluronic F127 (EO$_{106}$PO$_{70}$EO$_{106}$, BASF) triblock copolymer used as the structure directing and the corresponding amount of water and HCl 2 M were mixed under stirring. After dissolution, TEOS was added and allowed to react at room temperature for about 24 h. Then, the mixture was transferred into polypropylene bottles and heated at 80 °C for 48 h. The solid residue was filtered, washed and dried at room temperature and then at 110 °C for 24 h. Finally, the sample was calcined at 550 °C in air for 6 h.

The support modification with phosphate was performed employing the post-synthesis method (grafting). Typically, the SBA-15 or SBA-16 materials were impregnated with aqueous solutions of H_3PO_4 of appropriate concentrations to obtain substrates with P_2O_5 loadings of 0.5, 1.0, 1.5, 2.0 wt%. After water evaporation at room temperature, the solid was dried at 110 °C for 4 h and then calcined at 500 °C for 4 h.

2.2. Catalyst preparation

Two series of CoMoW catalysts were prepared using the P-free and P-containing SBA-15 and SBA-16 substrates. Each support was loaded with fixed amounts of molybdenum (8.53 wt% as MoO_3), tungsten (13.75 wt% as WO_3) and cobalt (3.81 wt% as CoO), by simultaneous impregnation via incipient wetness method. For this, an aqueous solution containing ammonium heptamolybdate tetrahydrate (($NH_4)_6Mo_7O_{24}\cdot4H_2O$, Aldrich), ammonium meta-tungstate (($NH_4)_6H_2W_{12}O_{40}\cdot xH_2O$, Aldrich) and cobalt nitrate hexahydrate (Co($NO_3)_2\cdot6H_2O$, Aldrich, 98%) was prepared. The concentrations were calculated to achieve a Mo/W atomic ratio of 0.5 and a Co/Mo atomic ratio of 0.3. The impregnates were dried at 85 °C for 16 h and then calcined at 500 °C for 4 h.

2.3. Characterization techniques

2.3.1. Chemical analysis

The chemical analysis of the catalysts (wt%) was measured by the EDAX method (a JEM 2100F microscope) taking into account average of five measurements at different points of the solid material. Less than 20% deviation from the average value was obtained from the average value obtained in EDAX values for all catalysts studied.

2.3.2. N$_2$ adsorption–desorption isotherms

The textural properties of the oxide catalysts and bare supports were determined from the adsorption–desorption isotherms of nitrogen at −196 °C, recorded with a Micromeritics TriStar 3000 apparatus. Prior to the experiments, the samples were degassed at 270 °C in vacuum for 5 h. The volume of the adsorbed N$_2$ was normalized to the standard temperature and pressure. The specific areas of the samples were calculated by applying the BET method to the nitrogen adsorption data within the 0.005–0.25 P/P_0 range. In order to avoid the tensile strength (TSE) artifact, the pore size distribution (PSD) curves were calculated by applying the Barret-Joyner-Halenda method (BJH) to the adsorption branches of the N$_2$

isotherms. The total pore volume (V_t) was obtained from the isotherms at $P/P_0 = 0.99$.

2.3.3. X-ray diffraction (XRD)

The pure supports and calcined catalysts were characterized by powder X-ray diffractometry according to the step-scanning procedure (step size 0.02°; 0.5 s) with a computerized Seifert 3000 diffractometer, using Ni-filtered CuKα ($\lambda = 0.15406$ nm) radiation and a PW 2200 Bragg-Brentano $\theta/2\theta$ goniometer equipped with a bent graphite monochromator and an automatic slit. The assignment of the various crystalline phases was based on the JPDS powder diffraction file cards.

2.3.4. DRS UV–vis

The UV–vis diffuse reflectance spectra of the calcined catalysts were recorded in the range of 200–800 nm at room temperature using a Varian Cary 5000 UV–vis spectrometer equipped with an integration sphere.

2.3.5. Micro-Raman

Micro-Raman spectra were recorded in a commercial micro-Raman system (Dilor Labram Model) equipped with a 20 mW He-Ne laser emitting at 632.8 nm, and a holographic notch filter from Kaiser Optical Systems, Inc. (model Super Notch-Plus). All Raman spectra were recorded at room temperature.

2.3.6. Temperature programmed reduction and desorption studies

The reduction behavior of the calcined catalysts was studied by temperature-programmed reduction (TPR) using a Micromeritics TPR/TPD 2900 instrument provided with a TCD and interfaced to a data station. The catalyst (0.05 g) was placed on a porous plate mounted in a 6.3 mm ID U-shaped quartz tube. Prior to reduction, the catalysts (ca. 50 mg) were heated at a rate of 15 °C/min up to a final temperature of 250 °C, and kept for 0.5 h at that temperature under a flow of He to remove water and other contaminants. The catalysts were cooled to ambient temperature in the same flow of He; then reduced in flowing gas containing 10% vol. H_2 in Ar at a total flow rate of 50 ml/min, and finally heated at a rate of 15 °C/min up to a final temperature of 1100 °C.

The acidity of the calcined catalysts was determined by temperature-programmed desorption (TPD) of ammonia measurements carried out with the same apparatus described for TPR. After loading, the sample of 0.050 g was pretreated in a He (Air Liquide, 99.996%) stream at 250 °C for 1 h. Following this, the sample was cooled to 100 °C and ammonia-saturated in a stream of 5% NH_3/He (Air Liquide) flow (50 mL/min) for 1 h. Then, after catalyst equilibration in a helium flow at 100 °C for 15 min, the ammonia was desorbed using a linear heating rate of 15 °C min⁻¹ to 1100 °C. In order to determine the total acidity of the catalyst from its NH_3 desorption profile, the area under the curve was integrated. A semiquantitative comparison of the acid strength distribution was made by Gaussian deconvolution of the peaks. Weak, medium and strong acidities were defined as the areas under the peaks having maxima in temperature intervals of 100–250 °C, 250–400 °C and 400–800 °C, respectively.

2.3.7. Transmission electron microscopy

The sulfide catalysts were studied by high-resolution transmission electron microscopy (HRTEM) using a JEM 2100F microscope operating with a 200 kV accelerating voltage and fitted with an INCA X-sight (Oxford Instruments). The catalysts were ground into a fine powder and dispersed ultrasonically in hexane at room temperature. Then, a drop of the suspension was put on a lacey carbon-coated Cu grid. At least ten representative images were taken for each sample. In order to obtain statistically reliable information, the length of ca. 250 particles was measured. Particle size distribution was evaluated from several micrographs taken from the same sample. The average particle size was estimated considering the statistical analysis of the particle sizes distribution.

2.3.8. X-ray photoelectron spectroscopy (XPS)

X-ray photoelectron spectra of the fresh sulfided catalysts were recorded with the aim to study the degree of sulfidation of the supported species. VG Escalab 200R spectrometer equipped with a hemispherical electron analyzer and a Mg Kα ($h\nu = 1253.6$ eV) X-ray source was used. The catalyst sulfidation procedure was the same as those employed for catalyst activation before reaction (*vide infra* Section 2.4). The freshly sulfided CoMoW catalysts, which were kept under *i*-octane in order to avoid exposure to air, were first placed in a copper holder mounted on a sample-rod in the pretreatment chamber of the spectrometer and then outgassed at 130 °C for 1 h before transfer to the analysis chamber. The catalysts were outgassed at 10^{-5} mbar and then transferred to the ion-pumped analysis chamber, where residual pressure was kept below 7×10^{-9} mbar during data acquisition. The binding energies (BE) were referenced to the C 1 s peak (284.9 eV) to account for the charging effects. The areas of the peaks were computed after fitting of the experimental spectra to Gaussian/Lorentzian curves and removal of the background (Shirley function). Surface atomic ratios were calculated from the peak area ratios normalized by the corresponding atomic sensitivity factors.

2.3.9. Quantification of coke deposit

The amount of coke deposited on the spent catalysts was determined with thermogravimetric TGA/SDTA851 equipment (Mettler Toledo), measuring the weight change in the coked catalysts during temperature-programmed oxidation (TPO). Each sample (ca. 30 mg) was previously heated in order to homogenize coke and remove the volatile compounds up to 500 °C for 1 h in N_2 (10 °C min⁻¹; 200 mL min⁻¹ flow-rate). Once the sample was cooled to 30 °C (5 °C min⁻¹) a burning of coke was carried out by raising sample temperature to a final temperature of 900 °C at a rate of 10 °C min⁻¹ in a 20% O_2/N_2 gas mixture (50 mL min⁻¹). The amount of coke (+reactant/products mixture in the pores of catalyst) present in the spent catalyst was calculated by the difference between initial and final weight of the catalyst sample, with the initial weight taken as the mass of the sample after pretreatment at 500 °C under N_2 at 1 h.

2.4. Catalytic activity measurements

In this work, the HDS of DBT was carried out in a Parr model 4575 high-pressure batch reactor. In order to minimize internal diffusion limitations, all catalysts were thoroughly ground in a mortar to a fine powder. Prior to the catalytic test, the catalysts were sulfided *ex situ* at atmospheric pressure in a tubular furnace heated up 400 °C (4 °C/min) under a flow of H_2S in hydrogen (15%) and kept under those conditions for 4 h. Then, the sample was cooled down to room temperature under a nitrogen flow. All catalysts (including the reference sample) were sulfided by the same procedure. The sulfided catalyst (ca. 0.5 g) was then introduced into the batch reactor containing a solution of 5% vol of DBT in decaline ([DBT]$_0$ = 0.239 mol/L]. The reactor was then pressurized to 3.1 MPa with hydrogen and heated up to 350 °C at a rate of 10 °C/min. The stirring rate of the reaction mixture was sufficiently intense (600 rpm) to exclude external diffusion limitations. After the working temperature was reached, sampling for chromatographic analysis was performed during the course of each run to determine conversion versus time dependence. The reaction time was averaged to 5 h. The resulting products were analyzed using a HP 4890 gas chromatograph provided with a 10-ft packed column containing 3% OV-17 as separating phase on

Chromosorb WAW 80/100. The main reaction products from the HDS of DBT are biphenyl (BP), cyclohexylbenzene (CHB) and tetrahydrodibenzothiophene (THDBT). The comparison of selectivity was made for the catalysts recording the same DBT conversion (ca. 30%) at different reaction times. The total DBT conversion was calculated as DBT disappearance, and direct desulfurization (DDS) and hydrogenation (HYD) selectivities were defined as:

$$DDS : \frac{(BP) \times 100\%}{(CHB + BP + THDBT)} \quad (1)$$

$$HYD : \frac{(CHB + THDBT) \times 100\%}{(CHB + BP + THDBT)} \quad (2)$$

HDS kinetic rate constants (k) were calculated assuming pseudo-zero order kinetics referred to initial DBT concentration, DBT Conversión (X_{DBT}) and reaction time (t), taking into account that the excess of hydrogen was employed, thus, its partial pressure could be considered as constant. The equation employed for k values calculation was:

$$[DBT]_0(1 - X_{DBT}) = kt \quad (3)$$

Additionally, an intrinsic activity was calculated according to following expression:

$$k = (mol_{DBT} \times X_{DBT})/(mmol\ Me \times s)[mol_{DBT} \times mmol_{Me}^{-1} \times s^{-1}]$$

where X is total DBT conversion at reaction time of 5 h and Me is total metal content (mmol Co + mmol Mo + mmol W). For comparative purposes, the HDS activity of a commercial CoMo/Al$_2$O$_3$ (AKZO KF-752; Mo = 14.2%; Co = 3.8%; P = 0.83%; S_{BET} = 223 m^2 g^{-1}; average pore diameter = 6.6 nm) provided by Akzo Nobel. This catalyst is less active than KF-757 developed more recently by the same manufacturer for ULSD purposes.

3. Results

3.1. Characterization of calcined precursors

3.1.1. Textural properties

In Fig. 1(A) and (B) the N$_2$ adsorption/desorption isotherms of the calcined catalysts are compared with their respective SBA-15- and SBA-16-based supports. For the SBA-15 series, the N$_2$ isotherms are of type IV and show a clear H$_1$ type hysteresis loops suggesting that those materials have very regular mesoporous channels (Fig. 1(A)). The pure supports show one step desorption branch, with high porosity characteristics, indicating the existence of an open pore structure. On the contrary, the SBA-15-based catalysts show two-step desorption branch due to metal oxide plugs inside the pores. Comparison of the isotherms of supports and catalysts revealed considerable shift in the relative pressure indicating the formation of new mesopores after metal loading into supports. On the other hand, the isotherms of all SBA-16-based samples have the shape of a typical SBA-16 isotherm showing a steep desorption step at relative pressure of ca. 0.42 linked with the presence of inkbottle-type pores (Fig. 1(B)) [28].

Analyzing the effect of phosphate incorporation, the comparison of the isotherms of P-modified SBA-15 and SBA-16 supports revealed no considerable shift in the relative pressure (P/P^0), in which hysteresis was observed for P-free SBA-15 and SBA-16 samples. This indicates that the pore diameters of both materials did not change significantly after phosphorous loading. Indeed, for both SBA-15- and SBA-16-based series the volume of N$_2$ adsorbed–desorbed changes very little going from P-free to P-containing material with a largest P content (2 wt%) indicating that the pores occlusion by P species did not occur (Table 1). For both SBA-15 and SBA-16 series, the comparison of the low-angle XRD patterns of pure supports with respective calcined catalysts confirmed that mesoporous structure of the (x)P-SBA-15 and (x)P-SBA-16 materials were preserved after metal loading (some examples
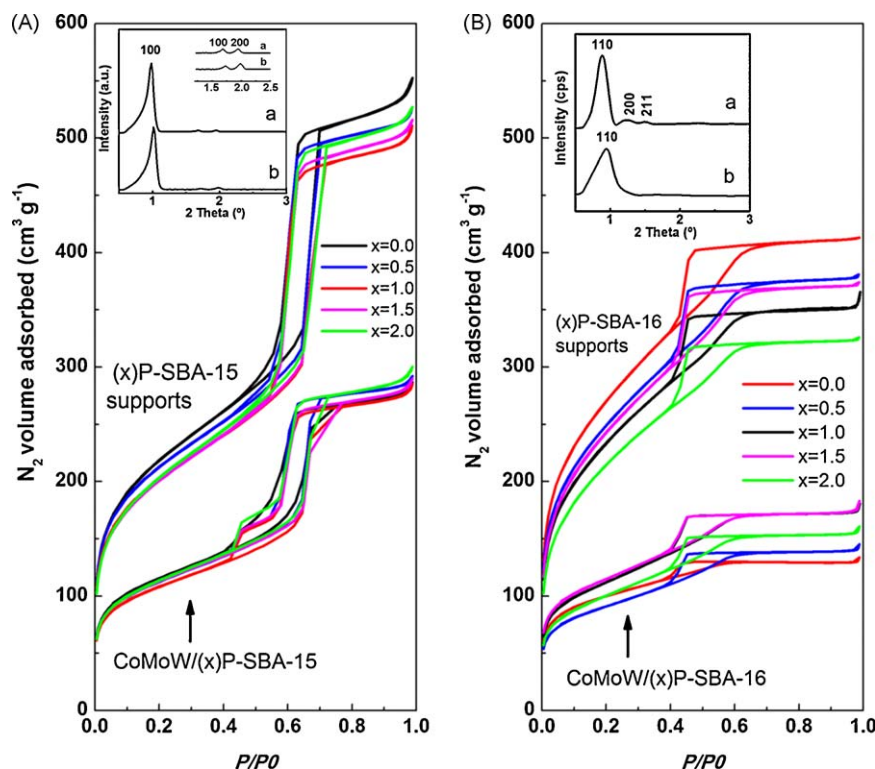

Fig. 1. Comparison of the N$_2$ adsorption–desorption isotherms of pure supports and calcined catalysts. Low-angle XRD patterns of the P-free support (a) and respective catalyst (b) are shown in inset of each figure.

Table 1
Textural properties of the calcined and fresh sulfided CoMoW/(x)P-SBA-15(SBA-16) catalysts and corresponding pure supports.

Sample x = wt% of P		S_{BET} (m^2 g^{-1})		Total pore volume (cm^3 g^{-1})		Pore diameter (nm)	
		SBA-15	SBA-16	SBA-15	SBA-16	SBA-15	SBA-16
P-free	Support	742	942	0.80	0.58	4.4	2.5
	Calcined	388	374	0.41	0.18	4.6	2.7
	Sulfided	223	208	0.28	0.14	5.1	2.6
x = 0.5	Support	717	869	0.76	0.54	4.4	2.5
	Calcined	380	366	0.42	0.21	4.5	2.7
	Sulfided	229	187	0.30	0.15	5.2	3.3
x = 1.0	Support	682	817	0.74	0.52	4.5	2.6
	Calcined	364	382	0.41	0.23	4.6	2.9
	Sulfided	208	296	0.29	0.22	5.5	2.9
x = 1.5	Support	682	852	0.75	0.54	4.5	2.5
	Calcined	381	389	0.41	0.23	4.6	2.7
	Sulfided	239	269	0.32	0.20	5.4	2.9
x = 2.0	Support	694	755	0.78	0.47	4.5	2.4
	Calcined	385	382	0.43	0.22	4.7	2.7
	Sulfided	333	211	0.40	0.16	4.8	3.1

Fig. 2. Pore size distribution of the fresh sulfided catalysts as determined from adsorption branch of the N$_2$ isotherm.

are shown in insets of Fig. 1(A) and (B)). Thus, the SBA-15-based materials show three well-resolved typical diffraction peaks, which are associated with a bi-dimensional p6mm hexagonal symmetry of the pores of SBA-15 material: one high-intensity peak at about $2\theta = 1.0°$ (1 0 0) and two low-intensity peaks at about $2\theta = 1.7$ and $2.0°$ corresponding to (1 1 0) and (2 0 0) reflections, respectively. The observed loss of peaks intensities could be due to decreasing contrast between walls and pores due to the filling of the pores, as described before [29]. Similarly, the low-angle XRD patterns of the SBA-16-based materials show three peaks corresponding to reflections indexes as (1 1 0), (2 0 0) and (2 1 1) [28] indicating that pore structure was preserved after metal oxides incorporation into SBA-16 material. After P-loading, the first most intense peak at 2θ of 0.86° becomes much broader indicating that the best structural ordering was achieved for the P-free SBA-16 material (figure not shown here).

The main textural properties of the bare supports, calcined and sulfided SBA-15- and SBA-16-based catalysts are listed in Table 1. As seen in this table, irrespectively of the support (SBA-15 vs. SBA-16), the support modification with phosphorous led to decrease in both specific surface area (S_{BET}) and total pore volume (V_t). Irrespectively of the P-loading, all SBA-16-based materials show a larger specific surface area (755–942 m^2/g) with respect to their SBA-15-based counterparts (682–742 m^2/g). For the SBA-15- and SBA-16-based materials, the average pore diameters are ca. 4.5 nm and 2.5 nm, respectively. The pore size distributions of the sulfided SBA-15- and SBA-16-based catalysts, calculated from the adsorption branch of N$_2$ isotherm, are shown in Fig. 2(A) and (B), respectively. As seen in Fig. 2(A), the sulfided CoMoW/(x)P-SBA-15 catalysts show a very narrow pore size distribution centred at about 6.2 nm. On the contrary, their SBA-16-supported counterparts show bimodal pore size distribution centred at about 2.8 and 4.3 nm. In general, regardless of the support, the loss of surface area due to the addition of P was rather small whereas the deposition of the active phases results in a dramatic decrease in the surface area. This is expected considering much smaller maximum phosphorous content in comparison with total metal loadings (2 vs. 26.1 wt%). Taking also into account that the size of pore diameter does not change significantly, one might to conclude that the introduction of the active phases followed by calcination resulted in the blocking of pores of the substrates. Indeed, the resulting decrease in surface area is more pronounced in the case of SBA-16 which has more narrow pores, than in case of SBA-15-
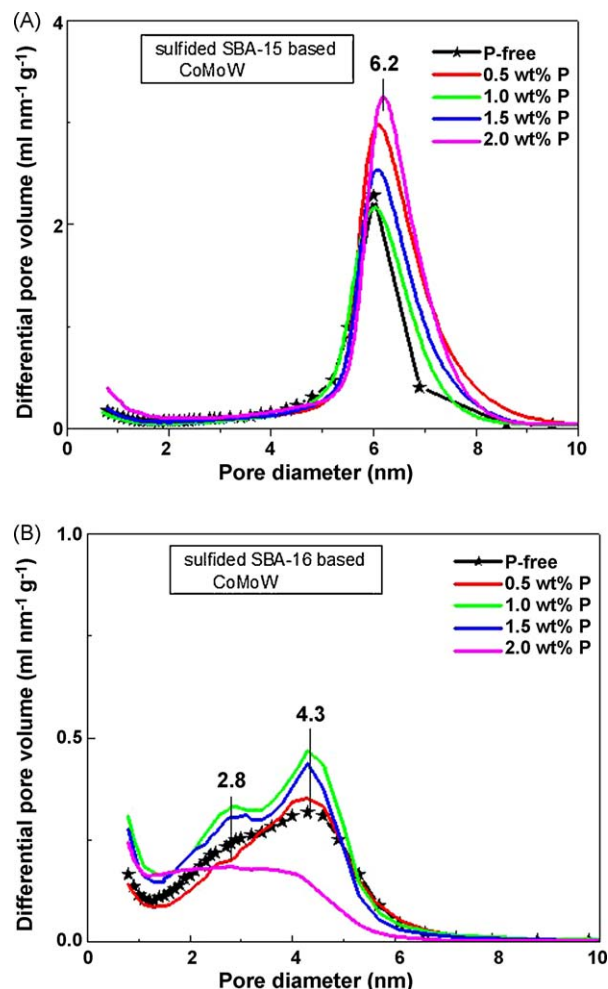
based catalysts. An increase in the pore diameter going from the support to the calcined catalysts could be explained considering that template were not completely removed during calcination of support whereas an increase in the pore diameter going from calcined to sulfided samples indicate that catalyst sulfidation led to segregation of metal oxide phases on the outer support surface. This explanation is consistent with the loss of specific surface area after sulfidation due to the blocking of pore's entrance by the clusters of metal oxides (Table 1).

In summary, results of nitrogen adsorption and pore size distribution analysis indicate that the presence of metal oxide clusters results in the blocking of pores of the substrates. The resulting decrease in surface area is more pronounced in the case of SBA-16 which has more narrow pores than SBA-15.

3.1.2. Wide-angle X-ray diffraction (XRD)

Wide-angle XRD profiles were recorded with the aim to investigate the presence of any crystallite species in the catalysts. Fig. 3(A) and (B) illustrates the diffraction profiles of the calcined CoMoW/(x)P-SBA-15 and CoMoW/(x)P-SBA-16 catalysts, respectively. All oxide catalysts reveal typical diffraction patterns, with a very broad peak at around $2\theta = 24°$, typical of amorphous silica [30]. Moreover, the XRD patterns of CoMoW/SBA-15, CoMoW/0.5P-SBA-15 and CoMoW/1P-SBA-15 catalysts, contain low peak intensities at $2\theta = 25, 28, 32.5, 38, 43, 48, 57$ y $59.5°$ corresponding to β-CoMoO$_4$ phase (JCPDS-ICDD 21-868). In addition, a low peak
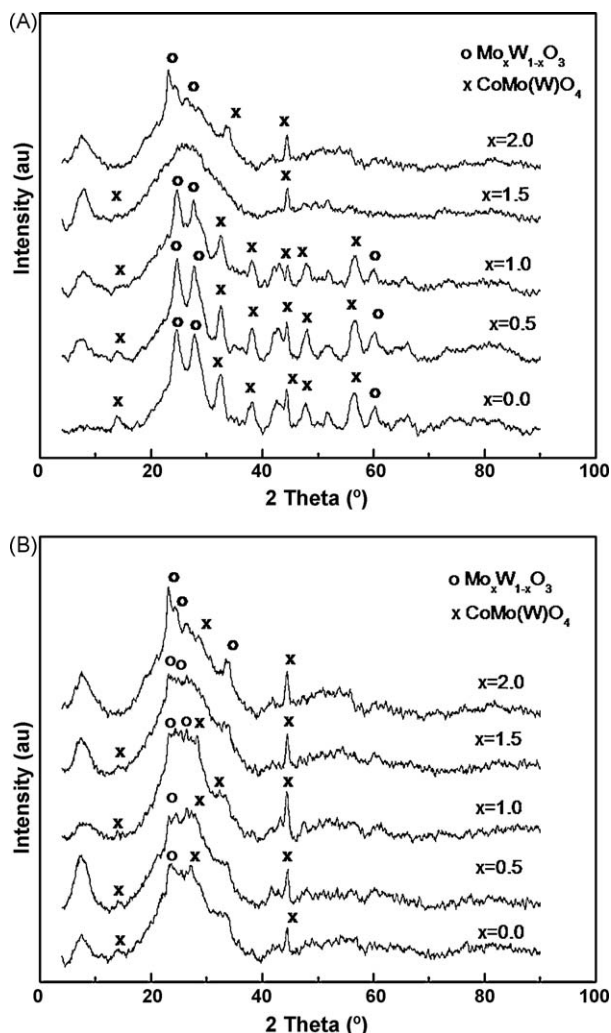
Fig. 3. Wide-angle XRD patterns of the calcined CoMoW/(x)P-SBA-15 (A) and CoMoW/(x)P-SBA-16 (B) catalysts (x = 0–2 wt% of P).
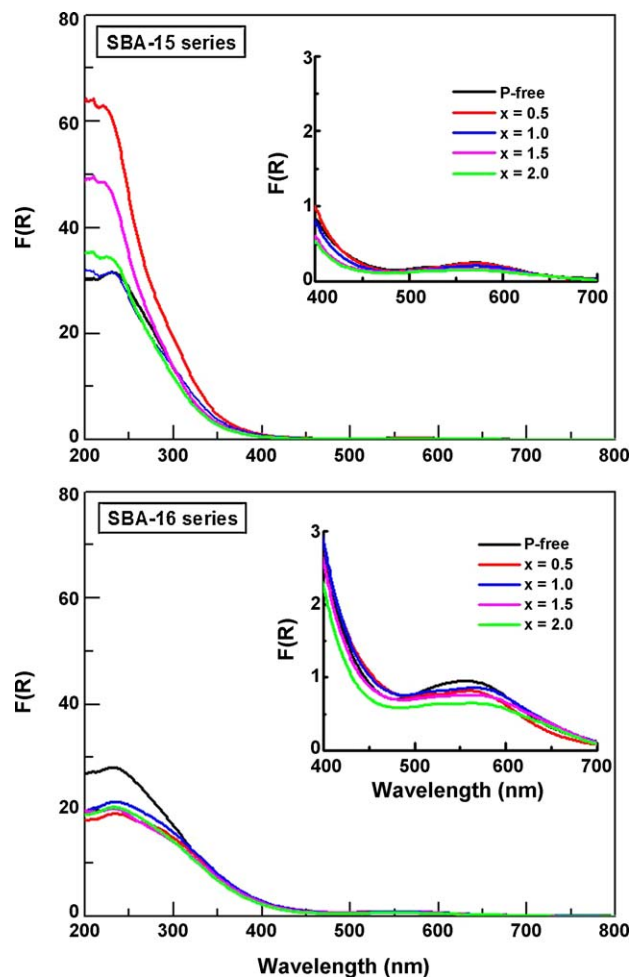
Fig. 4. UV–visible spectra of the calcined CoMoW/(x)P-SBA-15 and CoMoW/(x)P-SBA-16 catalysts in the ranges 200–450 nm and 400–700 nm (inset of each figure); x = wt% of P.

intensity at $2\theta = 43°$ was observed for SBA-16-based materials, CoMoW/1.5P-SBA-15 and CoMoW/2P-SBA-15 catalysts. The low intensity of the peaks indicates that most of the supported species should be widely dispersed on the surfaces of all catalysts. The CoMo(W)O$_4$ species might exist on the surface of the CoMoW/SBA-16 catalyst but they are amorphous or their crystal size is below the detection limit of XRD technique (<4 nm). In general, a better dispersion was observed for SBA-16-based catalysts. However, a slightly segregation of Mo$_x$W$_{1-x}$O$_3$ (JCPDS-ICDD 28-0668) phase is noticed, with exception of the CoMoW/1.5P-SBA-15 catalyst.

3.1.3. UV–vis diffuse reflectance spectra (DRS)

The coordination environment of Co^{2+} and Mo^{6+}(W^{6+}) ions in the calcined catalysts was studied by UV–vis diffuse reflectance spectroscopy. The DRS spectra of the calcined catalysts are plotted in Fig. 4 as a Kubelka-Munk-Schuster function. Regardless of the support and P-loading, all catalysts show two strong bands at about 210–270 nm and 320–350 nm. The first one imply the presence of a ligand-to-metal charge transfer involving isolated transition metal sites which is ascribed in literature to tungsten in tetrahedral coordination, like that in the WO$_4^{2-}$ group [31], but differed form that in the WO$_3$ crystal [32]. The second one is assigned in literature to O^{2-}-Mo^{6+} (W^{6+}) ligand-to-metal charge transfer transition (LMCT) of molybdenum and tungsten ions having octahedral coordination [33,34].

A displacement observed for the mentioned bands could be attributed to the influence of tungsten on the electronic properties of this kind of catalysts. It is noteworthy that all SBA-15-supported catalysts showed similar amount of Mo^{6+}(W^{6+}) ions in octahedral coordination and a larger amount of those ions in tetrahedral coordination than their SBA-16-supported counterparts. Concerning the phosphorus effect, one might note that after P incorporation into the CoMoW/SBA-16, the amount of the Mo^{6+}(W^{6+}) ions in tetrahedral coordination decreased suggesting the inhibition of the strong metal–support interaction by phosphorous species located on the support surface. Interestingly, for the SBA-15 supported catalysts, the phosphorus effect is opposite. Taking into account a larger pore diameter of the SBA-15 with respect to SBA-16 (4.6 vs. 2.7 nm) this is because the location of phosphorous species within the inner porous structure of the former catalysts which did not inhibit a strong metal–support interaction. As a consequence, for the SBA-15-supported catalyst the formation of the species having Mo^{6+}/W^{6+} ions in tetrahedral coordination is favored.

In contrast to the SBA-15-based catalysts, the visible spectra of the SBA-16-based catalysts exhibit bands in the 400–700 nm region (inset in Fig. 4), which are ascribed to d–d transitions (^{4}T$_{2g}$ to ^{4}A$_{2g}$ and ^{4}T$_{2g}$ to ^{4}T$_{1g}$ (P)) of high spin octahedral Co complexes [35,36]. The bands are very similar to those ascribed to both α- and β-CoMoO$_4$ compounds, in which Co is in an octahedral environment [35]. As shown in the inset in Fig. 4, the DRS spectra clearly

indicate that incorporation of P species into SBA-16 carrier diminish the amount of the Co tetrahedral species. Additionally, the DR spectra provide strong evidence that well-dispersed octahedral cobalt species are present on the surface of (x)P-SBA-16 substrates (shoulder at 525 nm). These species are easy reduced and sulfided, and therefore are susceptible to develop the HDS active sites [36,37].

3.1.4. Micro-Raman

Considering that Raman spectroscopy is effective for detecting the presence of crystalline as well as amorphous oxides, the calcined catalysts were studied by this technique. The Raman spectra of the SBA-15- and SBA-16-supported catalysts are shown in Fig. 5(A) and (B), respectively. For all catalysts, the absence of the band at about 1040–1060 cm^{-1} confirm that nitrate ions were completely removed by calcination at 500 °C for 4 h. CoMoW/1.5P-SBA-15 catalyst is unique one which show a very small peak at 1060 cm^{-1} indicative of the presence of traces of nitrate ions [38]. Regardless of the support and P-loading, Raman spectra of all catalysts show a major peak in the region between 900 and 1000 cm^{-1}. The broadness and position of this peak indicate the presence of several W and Mo species with different symmetries. Considering nominal metal loading of the catalysts studied (WO$_3$ = 13.75 wt%; MoO$_3$ = 8.53 wt%; CoO = 3.81 wt%), one might to expect that the mayor contribution to the intensity of this peak might to came from the W species. Thus, the band at around 960 cm^{-1} may arise from the W=O symmetric stretching vibration mode of W$_7$O$_{24}^{6-}$ species having W in the octahedral coordination [39]. Contribution from surface dioxo species Mo(=O)$_2$ species (970–975 cm^{-1}) [40] and Mo$_7$O$_{24}^{6-}$ species (948 cm^{-1}) [38] are also possible considering the broadness of the main peak. For all catalysts, the band at about 935 cm^{-1} could be ascribed as due to symmetric stretching vibrations of the W=O bond of tetrahedrally coordinated tungsten oxide hydrated species (WO$_4^{2-}$ ions) [41,42]. The formation of those species is confirmed also by the presence of peak at ~730–740 cm^{-1}, which is attributed to the asymmetric vibration of W^{6+}–O bonds (O–W–O stretching modes). Additionally, small features at 715 cm^{-1} and 435 cm^{-1} corresponding to WO$_3$ [43,44] and the band at ~510 cm^{-1} assigned to W–O–W linkages found in solvated polytungstates clusters [42] could be observed. Finally, considering the intermediate frequencies region, the band in the 200–300 cm^{-1} range corresponds to W − O − W bending modes of the bridging oxygen [45].

Concerning the Mo species, both SBA-15 and SBA-16 series show the band at ca. 983 cm^{-1} which is in the Mo–O–Mo stretching region of various polymolybdates havening irregular form (bankrupt, with a higher number of edge atoms) [46]. For the CoMoW/SBA-16 and CoMoW/0.5P-SBA-16 catalysts, the strong intensity of the band at 983 cm^{-1} indicates the presence of a large amount of polymerized Mo-oxide species. For SBA-16-based catalysts, the presence of the β-CoMoO$_4$ species is deduced from the band at 890 cm^{-1} (Mo–O–Co stretching vibrations) [38,47]. Moreover, the band at around 845 cm^{-1} can be associated with the asymmetric stretching mode of the Mo–O–Mo bridge bond of the octahedral molybdate species [38]. Finally, the band at about 820–825 cm^{-1} is due to Mo–O–Mo linkage in the orthorhombic MoO$_3$ [47].

To conclude, the Raman spectra demonstrated that both the phosphorus incorporation and the morphology of SBA-16 material favor the polymerization degree of the W and Mo species. Regardless of the support, the addition of small amount of phosphorous (0.5 wt%) led to the enhancement of the formation of polymolybdates havening bankrupt forms with a higher number of edge atoms as well as to the larger formation of W$_7$O$_{24}^{6-}$ species having W in the octahedral coordination.
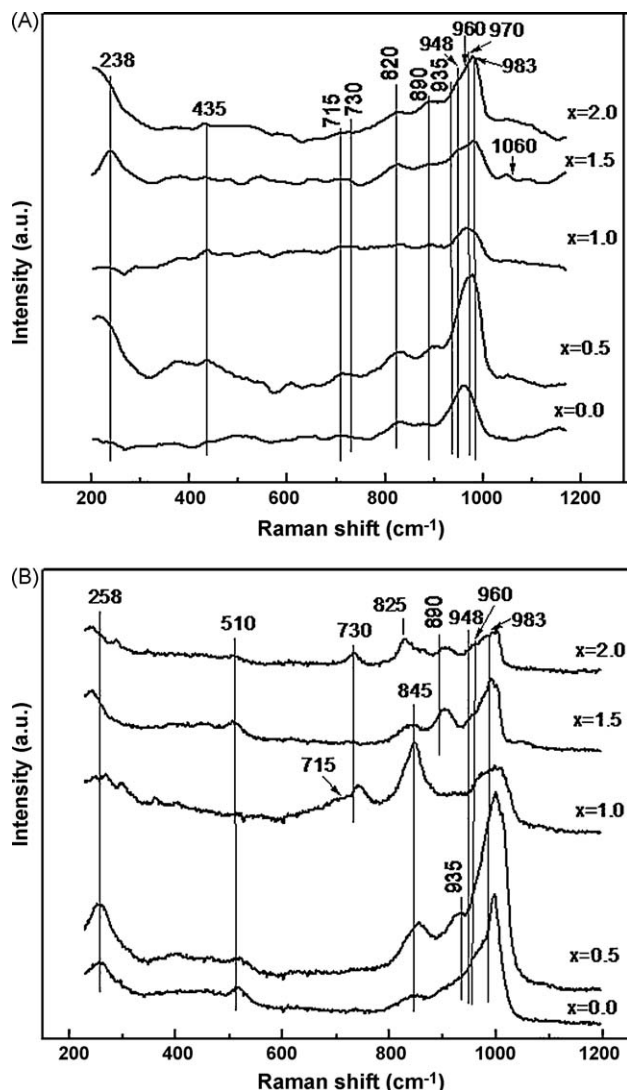

Fig. 5. Raman spectra of the calcined CoMoW/(x)P-SBA-15 (A) and CoMoW/(x)P-SBA-16 (B) catalysts (x = 0–2 wt% of P).

3.1.5. Temperature-programmed reduction (TPR)

Fig. 6 shows the TPR profiles of the calcined catalysts. The samples display quite similar TPR profiles although the tungsten incorporation modifies to some extent the reduction temperature of Mo oxide. However, these TPR profiles are different to the TPR profiles of the free tungsten catalysts, CoMo/SBA-15 and CoMo/SBA-16 [48]. Indeed, the tungsten presence in the catalysts provoke certain changes in the TPR profiles: (1) shifting of the two peaks reduction at higher temperatures, from 542 and 755 °C (to the free W catalysts) to 550 and 800 °C (to the catalysts containing W) and (2) decreasing in intensity of the first peak reduction and increasing in intensity of the second peak reduction. It can be stated that the tungsten incorporated in CoMo catalysts affects the reduction behavior of the catalysts resulting in a higher reducibility species, like tungsten in octahedral coordination.

Moreover, there is a strong influence of P-loading on the reduction profiles. The P-free catalysts show the lowest reduction temperature among the catalysts studied. The TPR profiles display a well-defined narrow peak at 500–550 °C and another broad one between 700–800 °C. The former is more intense and broad when P-loading increases. As cobalt species are reduced at lower temperatures than Mo(W)O$_3$, it is likely that free cobalt oxide species can contribute to the first H$_2$ consumption peak. The
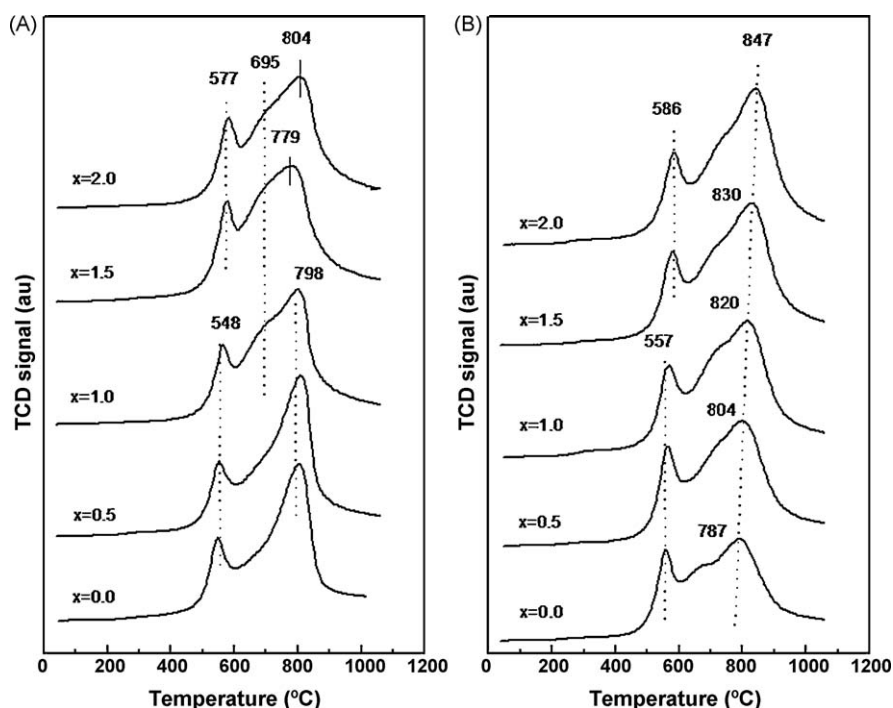
Fig. 6. TPR profiles of the calcined CoMoW/(x)P-SBA-15 (A) and CoMoW/(x)P-SBA-16 (B) catalysts (x = 0–2 wt% of P).

hydrogen consumption at ca. 550 °C was ascribed in literature for the reduction of very small Co particles strongly interacted with HMS [49]. In addition, the TPR profiles show some shoulders between the temperature intervals of 550–700 °C, which have often been ascribed to the reduction of Mo and W species interacting with Co [40,50–52]. Therefore, a strong Co–Mo–W interaction is expected to be developed in a common crystalline structure. Our TPR profiles are very similar to that reported by Herrera et al. [47] for CoMo/SiO₂. However, the presence of shoulders in the temperature interval of 550–700 °C could indicate the presence of a small amount of segregated WO₃ species which are generally reduced in this temperature range [50–52]. In order to get an idea of the degree of interaction of the supported phases with support, total H_2-consumption was determined (Table 2). As seen in this table, the CoMoW/SBA-15 shows larger H_2 consumption than the CoMoW/SBA-16. Regardless of the support used, P-loading induces an increase in H_2 consumption, in good agreement with literature [3]. However, P-loading on the SBA-16 led to a larger increase in H_2 consumption than in case of SBA-15-supported catalysts indicating a larger enhancement of the metal oxides reduction after P-loading on the former material. A similar trend was observed for the sulfidation degree as determined by XPS analysis (*vide infra*).

3.1.6. Temperature programmed-desorption of NH₃

The effect of support (SBA-15 vs. SBA-16) and P-loading (2.0 wt% of P) on the acidity of calcined catalysts was determined by NH₃-TPD. Fig. 7 compares NH₃-TPD profiles of both CoMoW/SBA-15 and CoMoW/SBA-16 catalysts before and after phosphate incorporation (2 wt% of P). The strength of the acid sites can be determined by the temperature at which the adsorbed NH₃ desorbs. Based on the desorption temperature, the acid sites were classified as weak (100–250 °C), medium (250–400 °C), or strong ($T > 400$ °C). The peaks were treated mathematically using Gaussian functions. The concentration of weak, moderate and strong strength acid sites (expressed as mmol of desorbed NH₃ per g of catalyst) are shown in Table 3. All catalysts show weak, medium and strong strength acid sites. The first two peaks in all

NH₃-TPD profiles are attributed to the weak ($T_{max} \approx 200$ °C) and moderate ($T_{max} \approx 300$ °C) Brønsted acid sites, respectively. For the P-containing catalysts, the presence of P-OH defect sites in the SBA-15 (SBA-16) matrix might contribute to an increase in the population of medium strength acid sites. For temperatures higher than 300 °C, ammonia desorption peaks probably corresponds to the structural acid sites [53] whereas the small peak observed at highest desorption temperature is probably due to the Lewis acid sites. From Table 3, one might conclude that the P-free CoMoW/SBA-16 catalyst possesses larger amount of weak and moderate strength acid sites and a lower amount of strong strength acid sites than its CoMoW/SBA-15 counterpart. On the contrary to SBA-15, phosphate incorporation to SBA-16 substrate leads to an increase in the amount of strong strength acid sites (Lewis acidity). However, irrespectively of the support, both P-containing catalysts showed the same total amount of acid sites. An increase in acidity after P-loading could be explained considering that the interaction of phosphoric acid at the SBA-15(SBA-16) surface occurs through formation of P(OH)₂–O–Si bonds or even free OP(OH)₃ entities interacting with the surface via H-bonding. For P/γ-alumina

Table 2
H_2 uptake ($\pm 2\%$) from TPR[a].

Sample	H_2 uptake (mmol/g cat)			
	I peak	II peak	III peak	Total
CoMoW/SBA-15 and CoMoW/(x)P-SBA-15				
P-free	0.8	3.2	1.7	5.7
x = 0.5	0.8	3.9	1.3	6.0
x = 1.0	0.9	1.4	3.4	5.7
x = 1.5	1.2	0.3	5.4	6.9
x = 2.0	1.2	1.0	3.9	6.1
CoMoW/SBA-16 and CoMoW/(x)P-SBA-16				
P-free	1.0	0.8	2.8	4.6
x = 0.5	1.1	0.9	4.0	6.0
x = 1.0	1.2	1.2	3.9	6.3
x = 1.5	1.1	1.3	3.4	5.8
x = 2.0	1.1	1.4	3.8	6.3

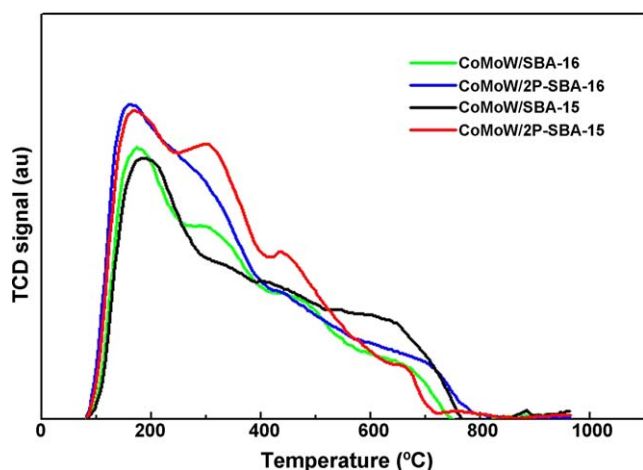[a] As obtained by Gaussian deconvolution of the TPR patterns.

Fig. 7. Influence of support (SBA-15 vs. SBA-16) and its modification with P (2.0 wt%) on the acidity of calcined catalysts as determined by TPD-NH$_3$.

materials, it was found that the different alumina hydroxyls react with H$_2$PO$_4$ preferentially depending on their basicity up to critical concentration of ca. 1×10^{12} H$_3$PO$_4$ cm^{-2}. The authors proposed that above this concentration H$_3$PO$_4$ reacts not only with Al–OH groups but also with P–OH groups to form polyphosphate species [54].

3.2. Characterization of fresh sulfide and spent catalysts

3.2.1. HRTEM measurements

Since metal sulfides are the active phases in HDS reaction, the fresh sulfided catalysts were studied by HRTEM. Concerning the support morphology, HRTEM images confirmed the regular porous arrangement of the SBA-15- and SBA-16-supported catalysts (Fig. 8(A)–(D)). Thus, SBA-15-based catalysts show the regular hexagonal opening of their channels (Fig. 8A) whereas SBA-16-based counterparts show regular pore structure along [1 0 0] (Fig. 8B) and [1 1 1] (Fig. 8C) direction corresponding to a cubic *Im3m* structure. In addition, some distorted and collapsed areas can be distinguished. For all catalysts, EDX microanalysis performed over several areas on the HRTEM micrographs of the sulfided catalysts show a non-uniform distribution of Co, Mo and W on the surface (Table 4). In general, the SBA-16-based catalysts possess two-times larger Co content than SBA-15-based ones and both P-containing catalysts showed larger W content than the respective P-free samples (Table 4).

It is known that both MoS$_2$ and WS$_2$ phases adopt a layered structure with a Mo(W) atoms situated in trigonal prismatic coordination sphere. As expected, after sulfidation all catalysts display the typical fringes of MoS$_2$ (WS$_2$) crystallites. The location of MoS$_2$ (WS$_2$) fringes on the channel's walls of SBA-15 substrate is shown in Fig. 8D. In Fig. 9 are compared high magnification Mo(W)S$_2$ sheets observed on P-free and P-containing SBA-15 and SBA-16-supported catalysts. For all catalysts, the arrangement of W(Mo)S$_2$ layers parallel to the substrate indicates the basal plane attachment. No edge-plane attachment was observed because

such species easily escape detection. In general, the SBA-16-based systems show higher W(Mo)S$_2$ slabs density than on their SBA-15 counterparts (Fig. 9). It is noteworthy that the SBA-15-based catalysts show the W(Mo)S$_2$ layers parallel to the surface and attached to the walls of channels (Fig. 8D) whereas their SBA-16-based counterparts show disordered curved fringes of the W(Mo)S$_2$ (Fig. 9).

More information on the morphology of phases formed can be revealed by statistical evaluation of about 250 particles from 12 HRTEM images. The distribution of slab length and stacking number of Mo(W)S$_2$ particles are shown in Fig. 10(A) and (B), respectively, whereas Table 4 summarizes the average length and stacking number of the Mo(W)S$_2$ particles. TEM data are evaluated as follows: (i), a little larger Mo(W)S$_2$ particles are formed on CoMoW/SBA-16 than on CoMoW/SBA-15 (5.1 vs. 4.7 nm); (ii), regardless of the support, P-loading leads to a small increase in the sizes of MoS$_2$ particles and these are somewhat larger for CoMoW/1.5P-SBA-15 than for CoMoW/1.5P-SBA-16 counterpart (5.6 vs. 5.4 nm); and (iii), the morphology of support and their modification with P did not influence on the number of stacking layers showing all catalysts a highly stacked layers of Mo(W)S$_2$ particles (4 ± 1 layers). Finally, for both P-free samples, the inter-layer spacing was similar and a little larger than those of the pure Mo(W)S$_2$ phase (0.65 vs. 0.62 nm). As opposite to the CoMoW/1.5P-SBA-15 sample, the presence of phosphate species on the surface of the CoMoW/1.5P-SBA-16 catalyst leads to a relatively large expansion of the inter-layer spacing (from 0.65 to 0.7 nm).

3.2.2. X-ray photoelectron spectroscopy

In order to investigate the modification undergone by phosphorous incorporation as well as the influence of support morphology on the surface exposure and nature of surface species, XPS analysis of the fresh sulfided catalysts was performed. For all catalysts, the Si 2p core level peak was close to 103.3 eV, which is characteristic of SiO$_2$ [11,55]. The chemical environment of silicon ions was not affected by the presence of other components. Table 5 compiles the binding energies (BE) values corresponding to the W 4f$_{7/2}$, Mo 3d$_{5/2}$, Co 2p$_{3/2}$, S 2p and P 2p core-levels. As expected, all freshly sulfided samples recorded a binding energy of 161.8–162.9 eV which is characteristic to the presence of S^{2-} species [56]. The absence of any signal corresponding to sulfate species (BE at 169.0 eV) indicates absence of catalyst contamination by oxygen during the transfer of the catalyst from the sulfiding reactor to the UHV analysis chamber of XPS apparatus. The binding energy of P 2p core-level of the all samples was ca. 134.0 eV. This BE value is much lower than that corresponding to P$_2$O$_5$ (135.2 eV) indicating that the phosphorus species remain highly dispersed on the support surface.

Fig. 11 shows the Co 2p, Mo 3d-S 2p and W 4f$_{7/2}$ core-level spectra of representative CoMoW/SBA-16 catalyst. The spectra of all catalysts reveal Co 2p$_{3/2}$ peak at a binding energy 778.0 ± 0.1 eV, which is close to that expected for segregated Co$_9$S$_8$ phase (778.5 eV) [57]. The formation of "CoW(Mo)S" phase could be ruled out because the BE of this phase is about 0.9 eV higher than of Co$_9$S$_8$ [58]. Thus, the chemical interaction of Co species with the edge sites of W(Mo)S$_2$ particles does not apparently takes place. For all catalysts, the Mo 3d$_{5/2}$

Table 3
Acid properties of the calcined catalysts as determined by TPD-NH$_3$.

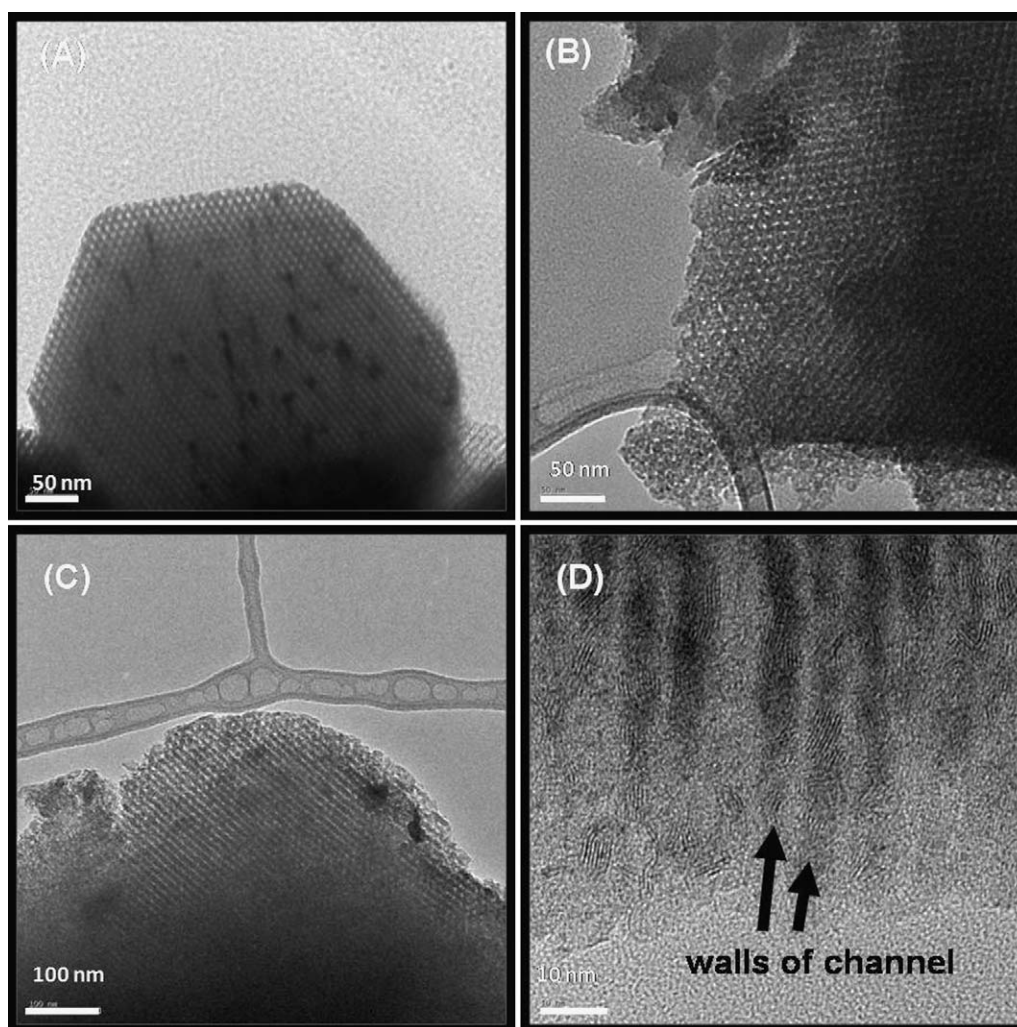| Sample	Amount of acid sites (mmol NH$_3 \times$ g$_{cat}^{-1}$)			
	Weak 100–250 °C	Moderate 250–400 °C	Strong 400–800 °C	Total
CoMoW/SBA-15	0.13	0.19	0.55	0.87
CoMoW/2P-SBA-15	0.20	0.40	0.44	1.04
CoMoW/SBA-16	0.18	0.28	0.36	0.82
CoMoW/2P-SBA-16	0.16	0.34	0.51	1.01

Fig. 8. HR-TEM images of fresh sulfided CoMoW/SBA-15 (A), CoMoW/SBA-16 (B) and CoMoW/1.5P-SBA-16 (C) catalysts showing their pore mouths and the location of Mo(W)S$_2$ fringes on the walls of CoMoW/1.5P-SBA-15 sample (D).

binding energy at 228.9 ± 0.1 eV is typical for Mo^{4+} in MoS$_2$ and an S $2p_{3/2}$ binding energy of 161.3 ± 0.6 eV is consistent with the S$_2^-$ type ligands present in MoS$_2$ [59]. Contrary to the molybdenum, the tungsten species were only partially sulfided in all catalysts. It is evident from the spectra that the binding-energy position of the W 4f$_{7/2}$ line remains constant for all catalysts. In order to estimate the fraction of sulfided W^{IV} species present on the both series of catalysts, the W 4f XPS signals were fitted assuming the coexistence of both sulfide and oxy-sulfide species. According to the literature [60] the W 4f peak at 32.0 eV corresponds to W^{IV} species in a WS$_2$-like structure while the other tungsten species with BE at 33.4 ± 0.1 eV may likely be associated with oxysulfide W species, which have both a terminal oxygen and a terminal sulfur. Similarly, EXAFS study of W L$_{III}$ edge showed that in sulfided W/SiO$_2$ catalysts part of the W ions contain oxygen atoms in the nearest environment resulting presumably from anchoring of sulfided particles to the oxygen of the support surface and thus forming W-O-Si linkages [61]. Considering the percentage of sulfided W species (given in parenthesis in Table 5), it appears that sulfidation degree of W species was relatively high (72–87%) for all catalysts. Unfortunately, no W^{3+} species could be determined from peak because the signal of W^{3+} ions strongly overlaps with the more intense signal coming from WS$_2$ species [62].

Table 4
Chemical composition (from EDX), HRTEM parameters of the fresh sulfided catalysts and reaction rate constants (k) at reaction time of 5 h.

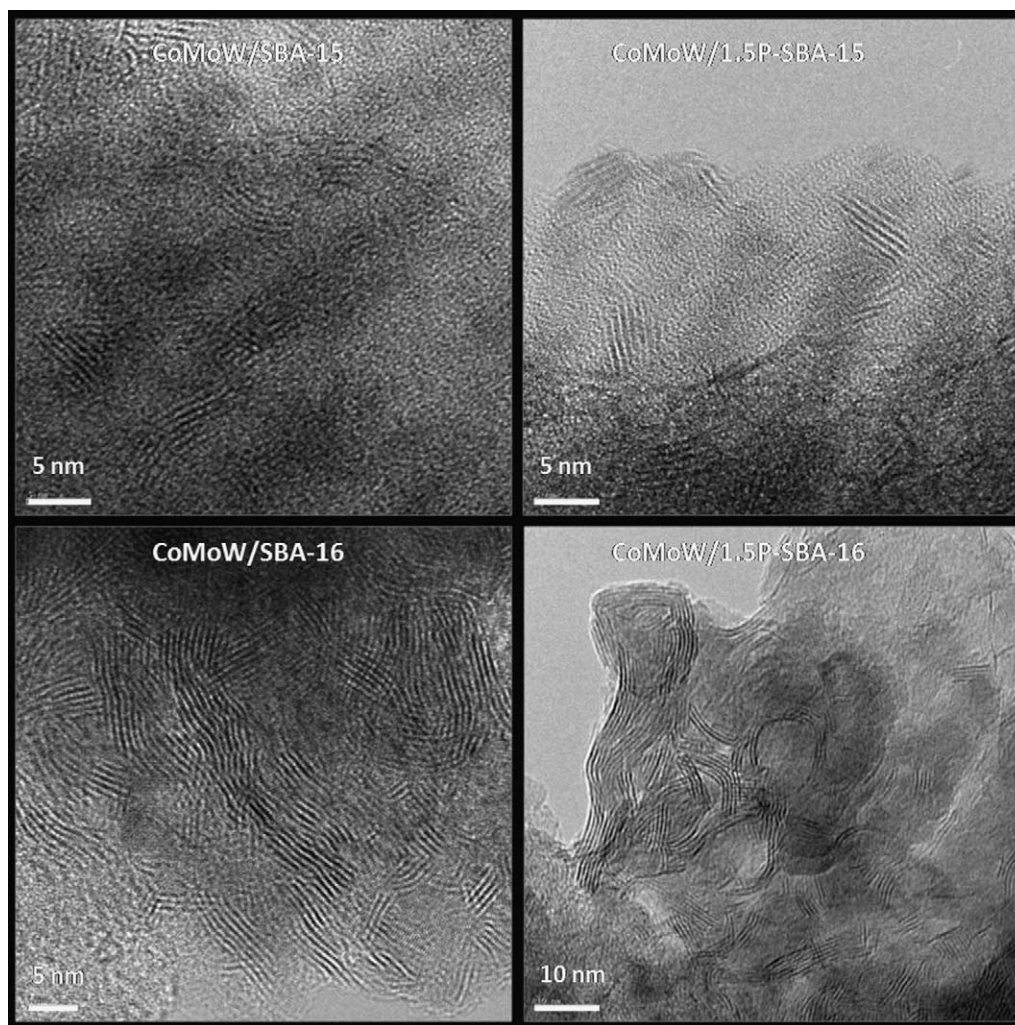|	CoMoW/SBA-15	CoMoW/1.5P-SBA-15	CoMoW/SBA-16	CoMoW/1.5P-SBA-16
Co (wt%)	3.2	2.2	7.0	5.1
Mo (wt%)	7.7	8.6	14.8	8.9
W (wt%)	18.5	24.0	17.7	22.3
P (wt%)	0.0	1.41	0.0	1.59
Average length (nm)	4.7	5.6	5.1	5.4
Stacking number	4 ± 1	4 ± 1	4 ± 1	4 ± 1
Surface density of Mo(W)S$_2$ particles (Mo(W)S$_2$/50 nm^2)	24 ± 4	21 ± 3	46 ± 4	42 ± 5
$k \times 10^{-6}$ (mol$_{DBT}$ g$_{cat}^{-1}$ s^{-1})	2.2	0.9	4.5	0.5
$k \times 10^{-6}$ (mol$_{DBT}$ mol Me^{-1} s^{-1})	0.3	0.27	0.3	0.24

Fig. 9. High magnification of Mo(W)S$_2$ sheets observed with freshly sulfided catalysts.

The distribution of supported Co, Mo and W species was estimated by comparing Co/Si, W/Si and Mo/Si atomic intensity ratios (Table 6). In general, it was found that the SBA-16-based catalysts showed larger Co, Mo and W surface exposure than their SBA-15-based counterparts. In particular, one might to note that the SBA-16-supported catalysts show two-times larger cobalt species surface exposure than the SBA-15-supported ones. Since all catalysts were prepared by the same method and employing similar conditions, one might to suppose that the lower cobalt species surface exposure could be due to their main location within inner porous structure of SBA-15. In order to confirm this, the bulk atomic ratios were calculated considering EDX data of chemical analysis (Table 4). The comparison of bulk and surface atomic ratios strongly suggested that: (i) regardless of support morphology, the cobalt sulfide species are mainly located on the external catalyst surface, (ii) contrary to the Co species, the Mo and W species are mainly located within the inner support structure; (iii) the P incorporation onto both SBA-15 and SBA-16 materials did not have a clear effect on the surface exposure of metal sulfide species.

3.2.3. Catalyst performance in HDS of DBT reaction

The HDS reaction of DBT was selected to test the activity of the SBA-15- and SBA-16-based catalysts. Fig. 12(A) shows the effects of both P-loading and support (SBA-15 vs. SBA-16) on the reaction rate constants at reaction time of 5 h. Both P-free CoMoW/SBA-15 and CoMoW/SBA-16 catalysts show the largest activity among the

catalysts studied being the latter catalyst more active than the former. Thus, it is clear that the use of the SBA-16 as support is more profitable than the use of SBA-15. For the catalysts having phosphate content larger than 0.5 wt%, the activity did not depend on the support morphology being a large phosphate content (2.0 wt%) clearly detrimental for both SBA-16 and SBA-15 materials. Considering the DBT conversion at $T = 350\,^{\circ}$C, $P = 3.1$ MPa and reaction time of 5 h, the most active CoMoW/SBA-16 catalyst displays larger activity than the commercial CoMo/Al$_2$O$_3$ catalyst (4.5×10^{-6} vs. 1.1×10^{-6} mol$_{DBT}$/g$_{cat}$ s).

To elucidate the influence of support morphology and the effect of phosphate incorporation on the SBA-15 and SBA-16 supports on the reaction pathways in HDS of DBT, in Fig. 12(B) are compared the product distributions at the same total DBT conversion (30%). The detailed analysis of the reaction products distributions indicates that the DBT conversion can take place through parallel direct desulfurization (DDS) and hydrogenation (HYD). For all catalysts, DDS route of DBT led to formation of biphenyl (BP) via hydrogenolysis whereas the HYD of one and two aromatic rings of DBT led to formation of tetrahydrodibenzothiophene (THDBT) and cyclohexylbenzene (CHB), respectively. BP was the main product indicating that for all catalysts the DDS route of DBT transformation is preferential. Contrary to the SBA-16-based catalysts, an increase in P-loading on the SBA-15-supported catalysts led to an increase in BP formation. With exception of CoMoW/SBA-16 and CoMoW/0.5P-SBA-16 catalysts, all catalysts show the formation of
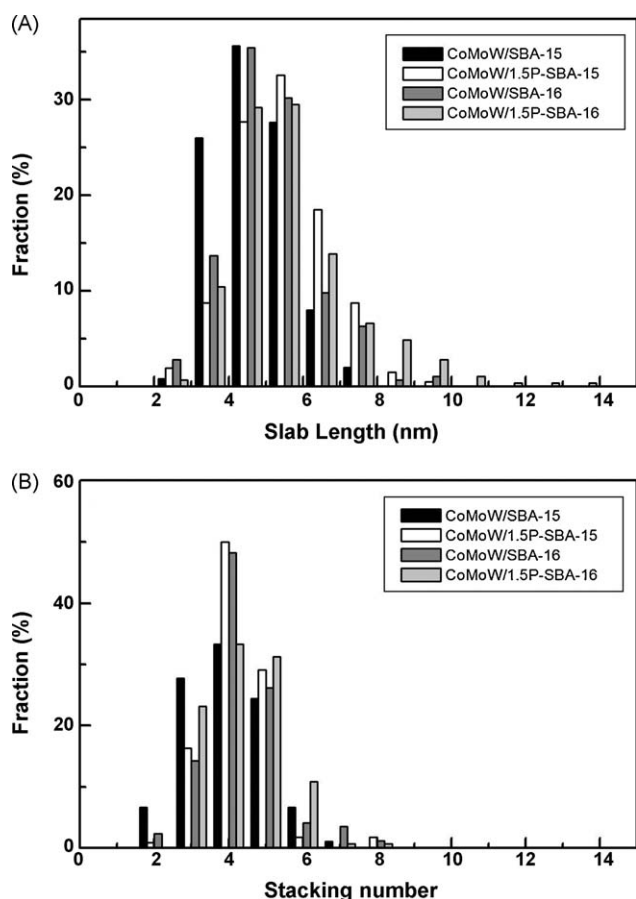
Fig. 10. Influence of support (SBA-15 vs. SBA-16) and its modification with phosphate (1.5 wt% of P_2O_5) on the distribution of slab length (A) and of stacking number (B) of Mo(W)S_2 particles as observed by HRTEM.

Table 5
Binding energies (eV) of the freshly sulfided catalysts.

Catalyst x = wt% of P	Co 2p$_{3/2}$	Mo 3d$_{5/2}$	W 4f$_{7/2}$	S 2p	P 2p
CoMoW/SBA-15 and CoMoW/(x)P-SBA-15					
P-free			32.1 (66)		
	778.0	228.9	33.6 (34)	162.0	–
x = 0.5			32.0 (75)		
	777.9	228.9	33.7 (25)	161.9	134.1
x = 1.0			32.1 (76)		
	778.0	228.9	33.8 (24)	162.0	134.2
x = 1.5			32.0 (63)		
	778.1	228.9	33.7 (37)	162.0	134.2
x = 2.0			32.2 (64)		
	778.0	229.0	33.7 (36)	161.9	134.2
CoMoW/SBA-16 and CoMoW/(x)P-SBA-16 series					
P-free			32.0 (75)		
	777.9	228.9	33.4 (25)	162.9	–
x = 0.5			31.9 (87)		
	777.9	228.9	33.4 (13)	161.8	134.0
x = 1.0			31.9 (82)		
	777.9	228.8	33.5 (18)	161.9	134.0
x = 1.5			32.0 (72)		
	777.9	229.0	33.3 (28)	161.8	134.0
x = 2.0			32.0 (72)		
	777.8	229.0	33.4 (28)	161.8	133.9

a small amount of THDBT. Hydrocracking products, such as benzene and cyclohexane, were not detected. In order to obtain more information about hydrogenation properties of the SBA-15- and SBA-16-based catalysts, the HYD/DDS selectivity ratio was calculated at the same DBT conversion (ca. 30%). HYD/DDS ratio of catalysts against their P_2O_5 loading is presented in Fig. 12(C). Contrary to the SBA-16-based catalysts, the P-loading onto SBA-15-supported catalysts, led to an increase in HYD/DDS ratio showing the CoMoW/2P-SBA-15 catalyst the largest hydrogenation among the catalysts studied.

Summarizing, in the HDS of DBT over sulfided CoMoW/(x)P-SBA-15 and CoMoW/(x)P-SBA-16 catalysts, the hydrogenolysis is dominant over hydrogenation. Irrespectively of the support, the incorporation of phosphate leads to a decrease in activity, being the sulfided CoMoW/SBA-16 catalyst most active among the catalysts studied (Fig. 12(A)). The phosphate addition into the SBA-15 substrate led to an increase in hydrogenation function, as deduced from an increase in the HYD/DDS ratio upon raising phosphate content (Fig. 12(C)). However, there was not correlation between catalytic activity and selectivity.

3.2.4. Coke quantification in spent catalysts

The influence of the support morphology (SBA-15 vs. SBA-16) as well as the effect of support modification by phosphate on the coking behavior of sulfided CoMoW catalysts in HDS reaction was evaluated from the weight change of the coked catalysts during temperature-programmed oxidation by means of TG-DTG technique. Figs. 13 and 14 present the TPO/TG-DTG plots of the spent SBA-15- and SBA-16-based catalysts, respectively, after 5 h of reaction time. Before the TPO analysis, the spent catalysts were pretreated at 500 °C for 1 h under flowing nitrogen to remove adsorbed reaction-mixture components. However, a period of 1 h was not enough taking into account the small weight loss in temperature range 30–300 °C attributed to desorption of reactant/ products adsorbed in the catalyst pores [63]. The second weight loss in the TG profiles, corresponding to most intense DTG peak centred at ~400 °C, can be assigned to lose of the sulfur atoms from oxo-sulfide species whereas the third weight loss (DTG peak centred at ~600 °C) is characteristic of coke oxidation [64]. Table 7 compiles the weight loss corresponding to the decomposition of metal sulfide species and oxidation of coke. Concerning the decomposition of the metal sulfide species, two observations could be made: (i) the metal sulfide phases of the CoMoW/SBA-15 catalyst are more stable than those of the CoMoW/SBA-16 counterpart; and (ii) P-loaded SBA-16 catalysts are more stable than their P-loaded SBA-15 counterparts. Concerning the oxidation of coke, similar amounts of coke were formed on P-free CoMoW/ SBA-15 and CoMoW/SBA-16 catalysts indicating that the catalyst morphology did not influence on the extent of coke formation. This situation is drastically changed after phosphate incorporation to both SBA-15 and SBA-16 substrates. For the SBA-15-based catalysts, the weight loss corresponding to coke burning follows the trend: 1.5P > 2P > 1P > 0.5P > P-free whereas for the SBA-16-supported ones the observed trend is: 0.5P = 1P > P-free -> 1.5P > 2P. Thus, for SBA-15-supported catalysts the phosphate addition led to an increase in coke formation whereas for the SBA-16-based catalysts the incorporation of a large amount of phosphate (1.5 and 2 wt% of P) followed an opposite trend.

4. Discussion

4.1. Effect of support morphology (SBA-15 vs. SBA-16)

Considering the HRTEM results, the higher reaction rate constant (expressed as mole of DBT converted per gram of catalyst and second) of the CoMoW/SBA-16 catalyst with respect to its
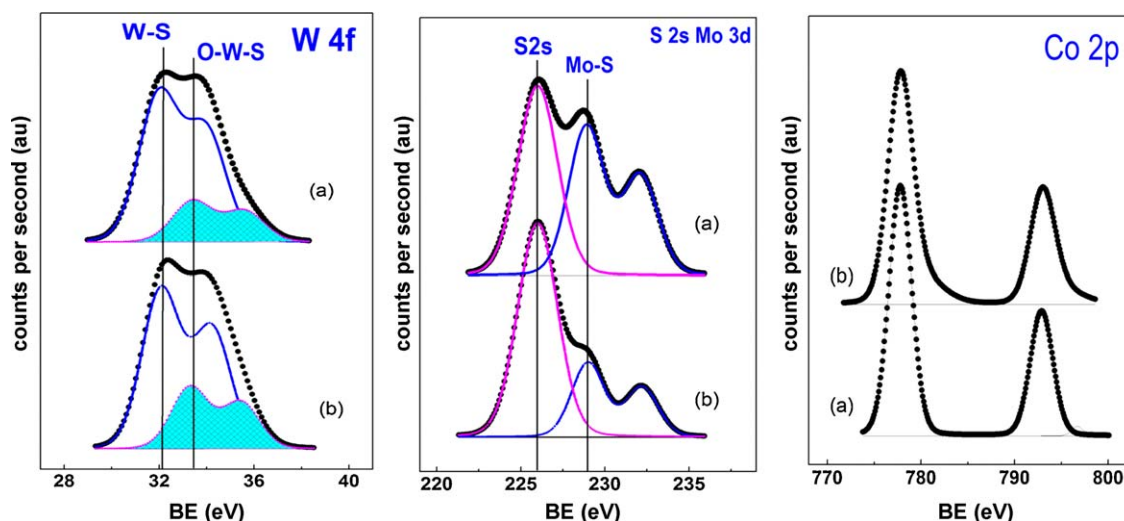
Fig. 11. W 4f, S 2s-Mo 3d and Co 2p core level spectra of the freshly sulfided CoMoW/SBA-16 (a) and CoMoW/2P-SBA-16 (b) catalysts.

CoMoW/SBA-15 counterpart (Fig. 12(A)) is due to the large density of the $Mo(W)S_2$ phases formed on the surface of the former catalyst (Fig. 9). For other CoMo catalyst systems (CoMo/P-HMS-Ti), we have observed a linear correlation between the surface densities of MoS_2 phases and their catalytic response in the HDS of DBT [11]. However, as shown in Table 4, this is not the case in this work indicating that factors other than the surface density of the $Mo(W)S_2$ phases may govern the catalytic activity. For the SBA-16-

based catalysts, the sulfidation of $CoMo(W)O_4$ phase results in segregation of Co_9S_8 crystallites and curved $Mo(W)S_2$ structures, as previously reported for sulfided $CoMoO_4$ phase supported on titania nanotubes [58]. Considering a larger density of $Mo(W)S_2$ slabs on the surface of the CoMoW/SBA-16 sample than on the CoMoW/SBA-15, the "ensemble effect" might be responsible for the catalytic activity of former catalyst. The ensemble effect, which is associated with particular arrangements of the active consti-

Table 6
Surface atomic ratios of the freshly sulfided catalysts.

Catalyst x = wt% of P	Co/Si at	Mo/Si at	W_{total}/Si at	W(S)/Si at	S/(Co + Mo + W) at	P/Si at
CoMoW/SBA-15 and CoMoW/(x)P-SBA-15 series						
P-free	0.052	0.013	0.010	0.007	1.66	–
	$(0.047)^a$	$(0.069)^a$	$(0.087)^a$			
x = 0.5	0.042	0.014	0.008	0.006	1.79	0.004
x = 1.0	0.049	0.009	0.007	0.0053	1.70	0.013
x = 1.5	0.046	0.013	0.010	0.006	1.61	0.012
	$(0.035)^a$	$(0.083)^a$	$(0.122)^a$			
x = 2.0	0.073	0.015	0.011	0.007	1.77	0.017
CoMoW/SBA-16 and CoMoW/(x)P-SBA-16 series						
P-free	0.101	0.034	0.015	0.011	1.73	0.00
	$(0.119)^a$	$(0.155)^a$	$(0.097)^a$			
x = 0.5	0.093	0.033	0.021	0.018	1.79	0.004
x = 1.0	0.110	0.047	0.033	0.027	1.75	0.011
x = 1.5	0.105	0.036	0.023	0.017	1.69	0.010
	$(0.083)^a$	$(0.089)^a$	$(0.116)^a$			
x = 2.0	0.131	0.020	0.012	0.009	1.70	0.009

[a] Bulk Co/Si, Mo/Si and W/Si values calculated considering EDX data (Table 4).

Table 7
Product distribution at DBT conversion of 30% and weigth loss during TPO of the spent catalysts (from TG).

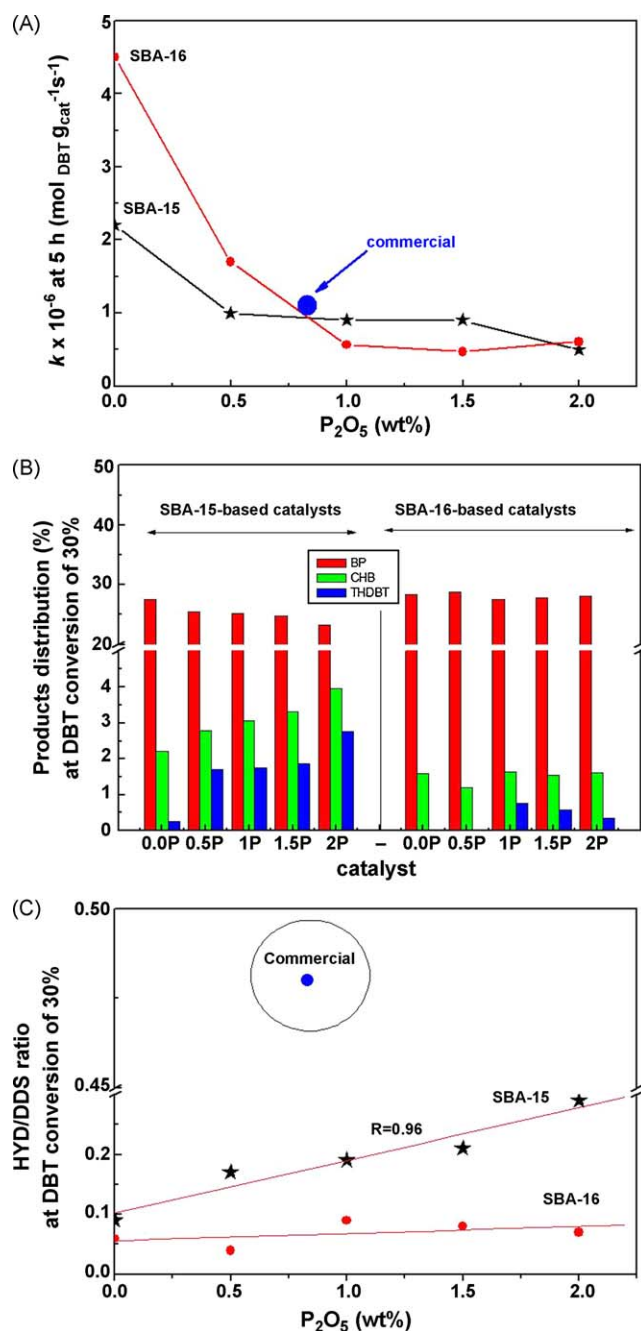| Catalyst x = wt% of P	Product distribution (wt%)				Weight loss (%)		
	BP	CHB	THDBT	T <320 °C	320 °C <T< 550 °C	T >550 °C	Total 30–800 °C
CoMoW/SBA-15 and CoMoW/(x)P-SBA-15							
P-free	27.51	2.21	0.27	0.8	1.5	2.0	4.3
x = 0.5	25.53	2.79	1.70	–	6.6	2.7	9.3
x = 1.0	25.18	3.06	1.75	–	3.8	4.4	8.2
x = 1.5	24.83	3.30	1.87	–	8.0	8.0	16.0
x = 2.0	23.29	3.94	2.75	–	7.0	7.0	14.0
CoMoW/SBA-16 and CoMoW/(x)P-SBA-16							
P-free	28.40	1.60	0.0	0.6	6.2	2.0	8.8
x = 0.5	28.79	1.21	0.0	0.5	4.4	2.2	7.1
x = 1.0	27.60	1.63	0.76	0.5	4.4	2.2	7.1
x = 1.5	27.85	1.55	0.59	0.4	3.0	1.7	5.1
x = 2.0	28.03	1.62	0.35	0.9	4.4	1.6	6.9

Fig. 12. HDS of DBT over sulfided CoMoW/SBA-15(SBA-16), CoMoW/(x)P-SBA-15(SBA-16) catalysts. Effects of phosphate loading and support morphology on the reaction rate constants (A), product distribution (B) and HYD/DDS selectivities ratio calculated at the same DBT conversion (30%) (C). For comparison, data of a commercial catalyst are included.

Fig. 13. TPO/TG-DTG plots of the spent CoMoW/(x)P-SBA-15 catalysts (x = 0–2 wt% of P).

tuents, was found to be extremely important for the adsorption, decomposition and chemical reaction of dibenzothiophene on surfaces of ternary catalysts such as e.g. RuNiMo [65].

The comparison of the bulk and surface Me/Si atomic ratio of the fresh sulfided CoMoW/SBA-15 and CoMoW/SBA-16 catalysts strongly suggests that W(Mo)S$_2$ and W sulfide species are mainly located in the inner catalyst structures (Table 6). Considering a large difference in the metal surface exposure between both catalysts (Table 6), the intrinsic activity was calculated (expressed as mole of converted DBT per mmole of metal and second). This calculation indicates that both P-free CoMoW/SBA-15 and CoMoW/SBA-16 catalysts show similar intrinsic activities in the HDS of DBT (Table 4). This strongly indicates that support
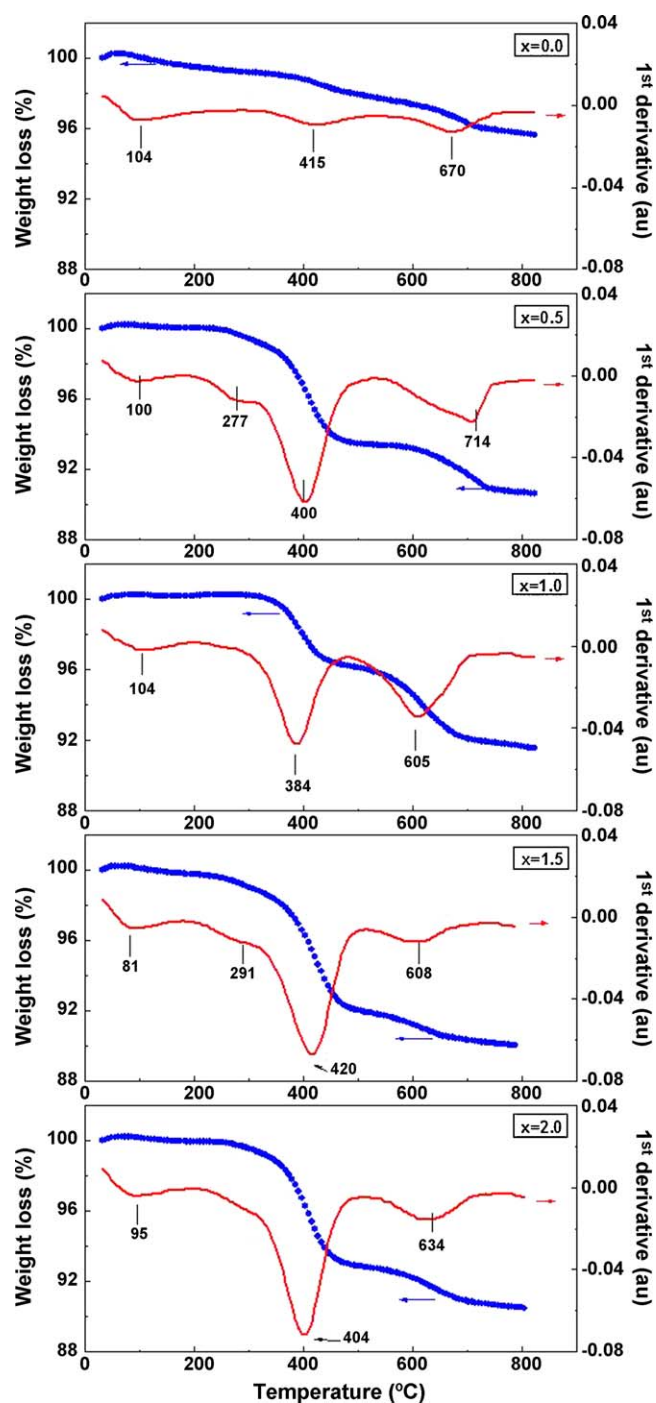
morphology did not control the catalytic response of those systems. This could be expected considering that reaction occurs mainly on the external catalyst surface. Thus, three dimensional channel connectivity of the SBA-16 substrate, which could provide more favorable mass transfer kinetics than the unidirectional pore system of the hexagonal mesoporous phases in the SBA-15, is not advantage for the DBT transformation over the SBA-16 catalysts.

4.2. Effect of phosphate addition

Regardless of the support, it was found that the addition of phosphorus has an inhibitor effect on the catalytic activity in the HDS of dibenzothiophene. Although both P-free CoMoW/SBA-15
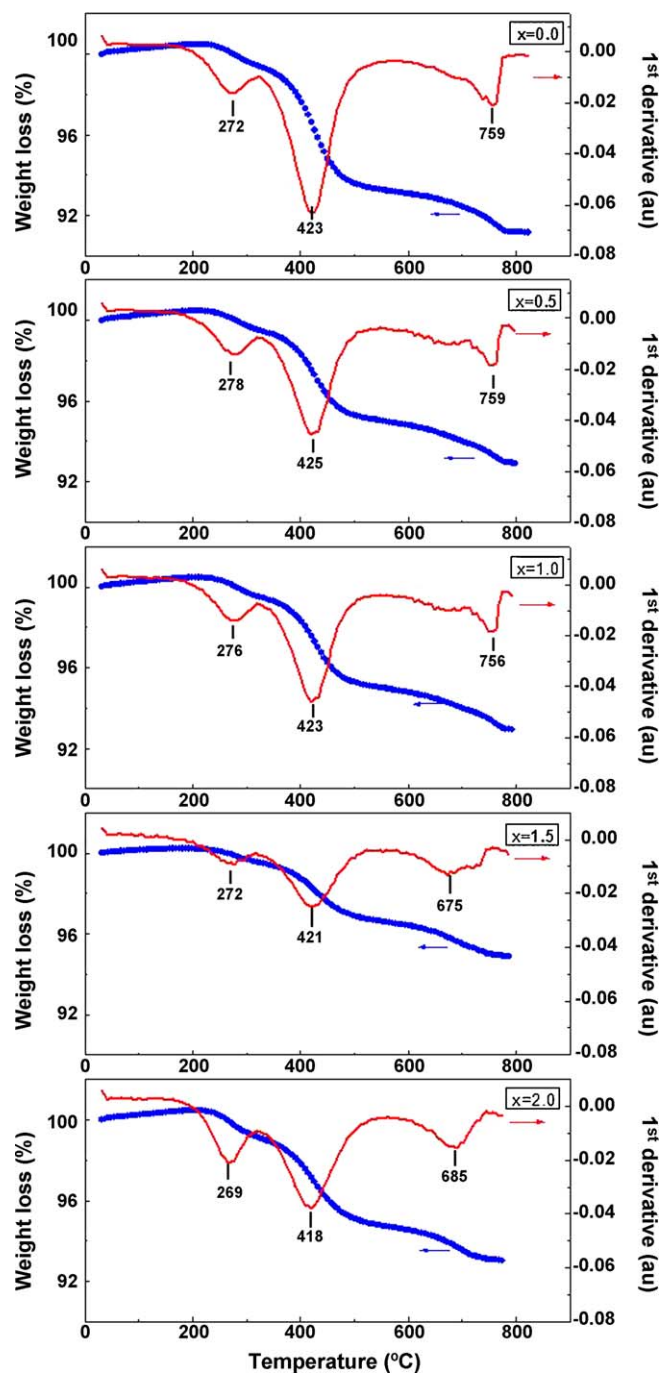
Fig. 14. TPO/TG-DTG plots of the spent CoMoW/(x)P-SBA-16 catalysts (x = 0–2 wt% of P).

contribute to an increase in coke formation. However, in this study there is no correlation between catalyst acidity and coke formation indicating that factors other than acidity might contribute to coke formation. Indeed, it was found that amount of coke diminished with an increase in metal sulfides surface exposure in the CoMoW/(x)P-SBA-15 (Fig. 15). Since for the SBA-16-based catalysts, modification with phosphorus led to inhibition of coke formation, for those catalysts a correlation between metal sulfides surface exposure and coke formation was not observed (Fig. 15).

The tentative explanation of a lower coke formation on the SBA-16-based catalysts with respect to the SBA-15-based ones assumes that coking is a "shape-selective" process [68]. Indeed, the "shape-selectivity" of coking was largely demonstrated for the zeolites being those with a medium pores (e.g. ZSM-5) much less deactivated than those with large pores [69]. Thus, contrary to the unidirectional pore system of the SBA-15, one might suppose that three dimensional channel connectivity as well as much lower pore diameter of the SBA-16 substrate could contribute to the inhibition of the coke deposition within inner porous structure of this material. Moreover, in case of the SBA-16-based catalysts, it is more likely that the presence of phosphate species on the support surface might prevent the formation of multipoint centres for coke adsorption, which are considered to be firstly deactivated by coke [70].

The SBA-15-based catalysts showed an increase in the HYD/DDS ratio raising phosphate content in the catalysts indicating an increase in HYD (Fig. 12(C)). Similar enhancement of HYD route in the HDS of DBT was observed for NiMo catalysts supported on MCM-41 [71] and for unsupported NiMoW catalysts [67] modified with phosphorus. Several explanations have been proposed in literature for the enhancement of hydrogenation character of the catalysts. For the unsupported NiMoW catalysts modified with P [67], it was concluded that the main effect of phosphorus was the loss of the nickel promotion effect by hampering the direct interaction between Ni and Mo(W) and leading to the segregation of nickel into highly crystalline nickel sulfide. Similarly, the enhancement of hydrogenation on the SBA-15-supported catalysts could be due, in part, to a lower cobalt promotion effect linked with lower cobalt loading on the SBA-15 than on SBA-16 counterparts, as derived from EDX and XRD. This is because cobalt promotion led to the enhancement of direct desulfurization route in the HDS of DBT [72]. Additionally, it is expected that phosphorus can destroy cobalt promotion effect when is incorporated directly into the W(Mo)S$_2$ slabs [73]. In this study, an increase in the stacking spacing of the MoS$_2$ (WS$_2$) layers after phosphate addition was deduced from HRTEM. This is possible considering that Mo(W)S$_2$ are layered compounds consisting of stacks of S-Mo(W)-S layers held together by van der Waals interactions [2]. Similar complex interactions between MoS$_2$ and WS$_2$ and P-modified support leading to decrease in van der Waals interactions was observed by us previously [9]. However, more detailed further experiments are needed in order to explain this phenomenon.

Finally, considering similar stacking degree of the W(Mo)S$_2$ crystallites in all catalysts studied by HRTEM (Table 4), the higher HYD on the SBA-15 series cannot be explained employing a rim-edge model which assumes that selectivity would change with the stacking degree of the W(Mo)S$_2$ fringes [74]. Similarly, if one consider the hypothesis by Iwata et al. [75], the onion-like curved W(Mo)S$_2$ particles of the SBA-16 might led to higher HYD than the non-curved fringes of the SBA-15-based catalysts but this is not our case. Thus, in good agreement with literature [67], we conclude that morphology of W(Mo)S$_2$ crystallites do not influence on the selectivity in the HDS of DBT.

Summarizing, for the SBA-16-based catalysts, addition of a large amount of P (>0.5 wt%) led to a decrease in the intensity of Raman band indicative of the presence of irregular clusters of the
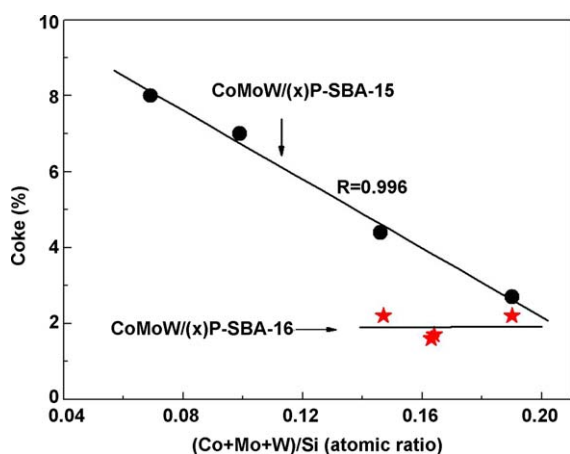
and CoMoW/SBA-16 catalysts showed higher HDS activity than a CoMo/Al$_2$O$_3$ commercial catalyst containing 0.83 wt% of P (Fig. 12(A)), the lower activity of the latter is more likely due to its much lower metal content than to its modification with phosphorus. The inhibition effect of phosphorus was reported also for cobalt-containing catalysts [66] and for unsupported NiMoW catalysts tested in the HDS of DBT [67].

For both SBA-15 and SBA-16 catalyst series, the inhibition of the HDS activity of catalysts by phosphorus seems to be the result of various cumulative effects leading to: (i) a decrease in metal–support interaction, as deduced from TPR; (ii) a decrease in specific surface area and pore volume due to a pore plugging phenomenon; and (iii) an increase in acidity (Table 3), which is known to

Fig. 15. Influence of the surface exposure of the metal sulfides (Co_9S_8, MoS_2, WS_2) (from XPS) on the inhibition of coke formation in the (x)P-SBA-15(16)-supported catalysts (x = 0.5, 1, 1.5 and 2 wt% of P).

metal oxides having a bankrupt structure with a higher number of edge atoms. Thus, it is concluded that the decrease in activity after phosphorus addition is due to the decrease in population of those species in the oxide precursors. Although the SBA-15 and SBA-16-supported catalysts could not be appropriate for ultra-low sulfur diesel applications owning their lower pore size than it is needed for the entrance of any methyl-substituted DBT molecules; useful information was obtained from the catalyst screening in the HDS of DBT. Although the trend in activity cannot be correlated with the textural properties (Table 1), the acid properties (Table 3), or more importantly with the support morphology, it was confirmed that the density of the active phases on the SBA-16 support surface (from combined HRTEM and XPS), together with the inhibitor effect of the phosphate on the coke formation, are two important factors which govern the HDS activity of CoMoW catalysts supported on mesoporous silica substrates.

5. Conclusions

The most significant results obtained by these studies can be summarized as follows: (i) the SBA-16 proved to be a better substrate to developing a large density of $Mo(W)S_2$ clusters on the surface than its SBA-15 counterpart; (ii) the P-free SBA-16 material is most optimized substrate for supporting Co, Mo and W phases; (iii) the irregular oxide Mo^{6+} and W^{6+} particles are precursors of the active phase formed upon sulfidation; (iv) regardless of the support morphology, the addition of phosphate was found to be detrimental for catalytic activity, so that new approaches are required for the application of phosphorus in the tailoring of novel hydrotreating catalysts supported on mesoporous siliceous materials; (v) for the SBA-16-based catalysts the presence of a large amount of phosphate (1.5 and 2.0 wt%) on the support surface inhibits coke formation during the HDS of DBT.

Acknowledgements

References

[1] Final Report by the European Commission on the Revision of Directive 98/70/EC.
[2] H. Topsøe, B.S. Clausen, F.E. Massoth, in: J.R. Anderson, M. Boudart (Eds.), Catalysts: Science and Technology, vol. 11, Springer, Berlin, 1997, pp. 111–191.
[3] M. Breysse, P. Afanasiev, Ch. Geantet, M. Vrinat, Catal. Today 86 (2003) 5.
[4] P.T. Vasudevan, J.L.G. Fierro, Catal. Rev. Sci. Eng. 38 (1996) 161.
[5] Y. Okamoto, M. Breysse, G. Murali Dhar, C. Song, Catal. Today 86 (2003) 1.
[6] R. Iwamoto, J. Grimblot, Adv. Catal. 44 (2000) 417.
[7] R. Nava, J. Morales, G. Alonso, C. Ornelas, B. Pawelec, J.L.G. Fierro, Appl. Catal. A: Gen. 321 (1) (2007) 58.
[8] R. Nava, B. Pawelec, J. Morales, R.A. Ortega, J.L.G. Fierro, Micropor. Mesoporous Mater. 118 (2009) 189.
[9] B. Pawelec, J.L.G. Fierro, A. Montesinos, T.A. Zepeda, Appl. Catal. B: Environ. 80 (2008) 1.
[10] B. Pawelec, T. Halachev, A. Olivas, T.A. Zepeda, Appl. Catal. A: Gen. 348 (1) (2008) 30.
[11] B. Pawelec, P. Castaño, T.A. Zepeda, Appl. Surf. Sci. 254 (2008) 4092.
[12] T. Halachev, R. Nava, L. Dimitrov, Appl. Catal. A. Gen. 169 (1998) 111.
[13] D. Trong On, D. Desplantier-Giscard, C. Danumah, S. Kaliaguine, Appl. Catal. A: Gen. 253 (2003) 545.
[14] A. Taguchi, F. Schüth, Micropor. Mesoporous Mater. 77 (2005) 1.
[15] Z. Kónya, E. Molar, G. Tasi, K. Niesz, G.A. Samoryani, I. Kirisci, Catal. Lett. 113 (2007) 19.
[16] W.J.J. Stevens, K. Lebeau, M. Mertens, G. Van Tendeloo, P. Cool, E.F. Vansant, J. Phys. Chem. B 110 (2006) 9183.
[17] Y. Sakamoto, M. Kaneda, O. Terasaki, D.Y. Zhao, J.M. Kim, G. Stucky, H.J. Shin, R. Ryoo, Nature 408 (2000) 449.
[18] C.F. Cheng, Y.-C. Lin, H.-H. Cheng, Y.-C. Chem, Phys. Lett. 382 (2003) 496.
[19] H. Ishihara, T. Itoh, T. Hino, M. Nomura, P. Qi, T. Kabe, J. Catal. 140 (1993) 184.
[20] A.J. Jacobson, R.R. Chianelli, T.A. Pecoraro, U.S. Patent 4,650,563 (1987).
[21] G. Alonso, M. Del Valle, J. Cruz-Reyes, A. Licea-Claverie, V. Petranovskii, S. Fuentes, Catal. Lett. 52 (1998) 55.
[22] D.J. Sajkowski, S.T. Oyama, Appl. Catal. A 134 (1996) 339.
[23] J. Bocarando, R. Huirache-Acuña, W. Bensch, Z.-D. Huang, V. Petranovskii, S. Fuentes, G. Alonso-Núñez, Appl. Catal. A: Gen. 363 (2009) 45–51.
[24] R. Huirache-Acuña, M.A. Albiter, J. Espino, C. Ornelas, G. Alonso-Nuñez, F. Para-guay-Delgado, J.L. Rico, R. Martínez-Sánchez, Appl. Catal. A: Gen. 304 (2006) 124.
[25] R. Huirache-Acuña, M.A. Albiter, C. Ornelas, F. Paraguay-Delgado, R. Martínez-Sánchez, G. Alonso-Nuñez, Appl. Catal. A: Gen. 308 (2006) 134.
[26] J. Bocarando, G. Alonso-Nuñez, W. Bensch, R. Huirache-Acuña, M. Del Valle, J. Cruz-Reyes, Catal. Lett. 130 (2009) 301–307.
[27] K. Flodström, V. Alfredsson, Micropor. Mesoporous Mater. 59 (2003) 167.
[28] D.Y. Zhao, Q.S. Huo, J.L. Feng, B.F. Chmelka, G.D. Stucky, J. Am. Chem. Soc. 120 (1998) 6024.
[29] F. Schüth, A. Wingen, J. Sauer, Micropor. Mesoporous Mater. 44–45 (2001) 465–476.
[30] R. Nava, R.A. Ortega, G. Alonso, C. Ornelas, B. Pawelec, J.L.G. Fierro, Catal. Today 127 (2007) 70.
[31] J.G. Graselli, B.J. Bulkin, Analytical Raman Spectroscopy, Wiley, New Cork, 1991, p. 352.
[32] Z. Zhang, J. Suo, X. Zhang, S. Li, Appl. Catal. A: Gen. 179 (1999) 11.
[33] R.A. Schoonheydt, in: F. Delannay (Ed.), Characterization of Heterogeneous Catalysts, Marcel Dekker, New York, 1984, p. 125.
[34] D.K. Lee, H.T. Lee, I.Ch. Lee, S.K. Park, S.Y. Bae, Ch.H. Kim, S.I. Woo, J. Catal. 159 (1996) 219.
[35] J.E. Herrera, D.E. Resasco, J. Catal. 221 (2004) 354.
[36] H.K. Matralis, Ch. Papadopoulou, A. Lycourghiotis, Appl. Catal. A: Gen. 116 (1994) 221.
[37] Ch. Papadopoulou, J. Vakros, H.K. Matralis, G.A. Voyiatzis, Ch. Kordulis, J. Colloid. Interface Sci. 274 (2004) 159.
[38] V. La Parola, G. Deganello, C.R. Tewell, A.M. Venezia, Appl. Catal. A 235 (2002) 195.
[39] A. Baserga, V. Russo, F. Di Fonzo, A. Bailini, D. Cattaneo, C.S. Casari, A. Li Bassi, C.E. Bottani, Thin Solid Films 515 (2007) 6465.
[40] E.L. Lee, I.E. Wachs, J. Phys. Chem. C 112 (2008) 20418.
[41] J.A. Horsley, I.E. Wachs, J.M. Brown, G.H. Via, F.D. Hardcastle, J. Phys. Chem. 91 (1987) 4014.
[42] M.A. Vuurman, I.E. Wachs, A.M. Hirt, J. Phys. Chem. 95 (1991) 9928.
[43] R. Huirache-Acuña, F. Paraguay-Delgado, M.A. Albiter, J. Lara-Romero, R. Martínez-Sánchez, Mater. Characterization 60 (2009) 932–937.
[44] M.F. Daniel, B. Desbat, J.C. Lassegues, B. Gerand, M. Figlarz, J. Solid State Chem. 67 (1987) 235.
[45] I.M. Szilàgyi, J. Mararàsz, G. Pokol, P. Király, G. Tárkányi, S. Saukko, J. Mizsei, A.L. Tóth, A. Szabó, K. Varga-Josepovits, Chem. Mater. 20 (2008) 4116.
[46] A.N. Desikan, L. Huang, S.T. Oyama, J. Phys. Chem. 95 (1991) 10050.
[47] P. Gajardo, P. Grange, B. Delmon, J. Phys. Chem. 83 (1979) 1771.
[48] R. Nava, M. Aguilar, B. Pawelec, J.L.G. Fierro, unpublished results.
[49] E. Lira, C.M. López, F. Oropeza, M. Bartolini, J. Alvarez, M. Goldwasser, F. López Linares, J.-F. Lamonier, M.J. Pérez Zurita, J. Mol. Catal. A: Chem. 281 (2008) 146.
[50] P.A. Clark, X. Wang, S.T. Oyama, J. Catal. 207 (2002) 256.
[51] P.A. Clark, S.T. Oyama, J. Catal. 218 (2003) 78.
[52] Y. Shu, S.T. Oyama, Carbon 43 (2005) 1517.

[53] P. Selvam, S.K. Mohapatra, Micropor. Mesoporous Mater. 73 (2004) 137.
[54] J.M. Lewis, R.A. Kydd, J. Catal. 132 (1991) 465.
[55] J. Finster, Surf. Interface Anal. 12 (1988) 309.
[56] C.D. Wagner, W.M. Riggs, L.E. Davis, J.F. Moulder, G.E. Muilenberg, Handbook of X-ray Photoelectron Spectroscopy, Perkin Elmer Corp, 1979.
[57] Y. Okamoto, T. Kubota, Catal. Today 86 (2003) 31.
[58] J.A. Toledo Antonio, M.A. Cortés-Jácome, C. Angeles Chávez, J. Escobar, M.C. Barrera-Domínguez, E. López-Salinas, Applied. Catal. B: Environ. 90 (2009) 213–223.
[59] A.F.H. Sanders, A.M. de Jong, V.H.J. de Beer, J.A.R. van Veen, J.W. Niemantsverdriet, Appl. Surf. Sci. 144–145 (1999) 380.
[60] S. Bendezú, R. Cid, J.L.G. Fierro, A. López Agudo, Appl. Catal. A: Gen. 197 (2000) 47.
[61] D.I. Kochubei, M.A. Kozlov, K.I. Zamaraev, V.A. Burmistrov, A.N. Startsev, Yu.I. Yermakov, Appl. Catal. 14 (1985) 1.
[62] K.T. Ng, D.M. Hercules, J. Phys. Chem. 80 (1976) 2094.
[63] B.N. Barman, L. Skarlos, D.J. Kushner, Energy & Fuels 11 (1997) 593.
[64] R.W. Soares, V.J. Menezes, M.V.A. Fonseca, J. Dweck, J. Thermal Anal. 49 (1997) 657.
[65] B. Pawelec, R.M. Navarro, P. Castaño, M.C. Álvarez-Galván, J.L.G. Fierro, Energy & Fuels 23 (2009) 1364.
[66] B.A. Kerns, O.A. Larson, U.S. Patent 3,446,730 (1969).
[67] H. Nava, J. Espino, G. Berhault, G. Alonso-Nuñez, Appl. Catal. A: Gen. 302 (2006) 177.
[68] B. Dimon, P. Cartraud, P. Magnoux, M. Guisnet, Appl. Catal. A. Gen. 101 (1993) 351.
[69] L.D. Rollmann, D.E. Walsh, J. Catal. 56 (1979) 139.
[70] K.G. Ione, G.V. Echeviskii, G.N. Nosyneva, J. Catal. 85 (1984) 287.
[71] B.-C. Kang, S.T. Wu, H.-H. Tsai, J.-C. Wu, Appl. Catal. 45 (1988) 221.
[72] P. Michaud, J.L. Lemberton, G. Pérot, Appl. Catal. A: Gen. 169 (1998) 343.
[73] O. Poulet, R. Hubaut, S. Kasztelan, J. Grimblot, Bull. Soc. Chim. Belg. 100 (1991) 857.
[74] M. Daage, R.R. Chianelli, J. Catal. 149 (1994) 414.
[75] Y. Iwata, K. Sato, T. Yoneda, Y. Miki, Y. Sugimoto, A. Nishijima, H. Shimada, Catal. Today 45 (1998) 353.